NASA TECHNICAL NOTE

NASA TN D-6833

NASA TN D-6833

SAFE ATMOSPHERE ENTRY OF AN ISOTOPE HEAT SOURCE WITH A SINGLE STABLE TRIM ATTITUDE AT HYPERSONIC SPEEDS

by Lionel L. Levy, Jr., and Raymond K. Burns

Ames Research Center
Moffett Field, Calif. 94035

NATIONAL AERONAUTICS AND SPACE ADMINISTRATION • WASHINGTON, D. C. • JUNE 1972

1. Report No.	2. Government Accession No.	3. Recipient's Catalog No.
NASA TN D-6833		

4. Title and Subtitle	5. Report Date
SAFE ATMOSPHERE ENTRY OF AN ISOTOPE HEAT SOURCE WITH A SINGLE STABLE TRIM ATTITUDE AT HYPERSONIC SPEEDS	June 1972
	6. Performing Organization Code

7. Author(s)	8. Performing Organization Report No.
Lionel L. Levy, Jr., and Raymond K. Burns	A-4342
	10. Work Unit No. 111-05-31-01-00-21

9. Performing Organization Name and Address	11. Contract or Grant No.
NASA Ames Research Center Moffett Field, Calif. 94035	
	13. Type of Report and Period Covered
12. Sponsoring Agency Name and Address	Technical Note
National Aeronautics and Space Administration Washington, D.C. 20546	14. Sponsoring Agency Code

15. Supplementary Notes

16. Abstract

A theoretical investigation has been made to design an isotope heat source capable of satisfying the conflicting thermal requirements of steady-state operation and atmosphere entry. The isotope heat source must transfer heat efficiently to a heat exchanger during normal operation with a power system in space, and in the event of a mission abort, it must survive the thermal environment of atmosphere entry and ground impact without releasing radioactive material. A successful design requires a compatible integration of the internal components of the heat source with the external aerodynamic shape. To this end, configurational, aerodynamic, motion, and thermal analyses were coupled and iterated during atmosphere entries at suborbital through superorbital velocities at very shallow and very steep entry angles.

Results indicate that both thermal requirements can be satisfied by a heat source which has a single stable aerodynamic orientation at hypersonic speeds. For such a design, the insulation material required to adequately protect the isotope fuel from entry heating need extend only half way around the fuel capsule on the aerodynamically stable (windward) side of the heat source. Thus, a low-thermal-resistance, conducting heat path is provided on the opposite side of the heat source through which heat can be transferred to an adjacent heat exchanger during normal operation without exceeding specified temperature limits.

17. Key Words (Suggested by Author(s))	18. Distribution Statement
Aerodynamic stability Entry heating	Unclassified – Unlimited

19. Security Classif. (of this report)	20. Security Classif. (of this page)	21. No. of Pages	22. Price*
Unclassified	Unclassified	51	$3.00

* For sale by the National Technical Information Service, Springfield, Virginia 22151

TABLE OF CONTENTS

Page

Page Intentionally Left Blank

NOTATION

C_A	axial-force coefficient, $\frac{2(\text{axial force})}{\rho V^2 S}$, dimensionless
C_N	normal-force coefficient, $\frac{2(\text{normal force})}{\rho V^2 S}$, dimensionless
C_Y	side-force coefficient, $\frac{2(\text{side force})}{\rho V^2 S}$, dimensionless
C_l	rolling-moment coefficient, $\frac{2(\text{rolling moment})}{\rho V^2 S l}$, dimensionless
C_m	pitching-moment coefficient, $\frac{2(\text{pitching moment})}{\rho V^2 S l}$, dimensionless
C_n	side-moment coefficient, $\frac{2(\text{side moment})}{\rho V^2 S l}$, dimensionless
C_p	pressure coefficient (eqs. (A2), (A3), and (A5)), dimensionless
F	nodal heating factor (eq. (E1)), dimensionless
$\overline{F}$	time-averaged nodal heating factor (eq. (E4)), dimensionless
h	heat-source height, m
$I_{x_B}, I_{y_B}, I_{z_B}$	moments of inertia about body axes x_B, y_B, z_B, kg-m^2
K	correction factor for three-dimensional stagnation point (eq. (D4)), dimensionless
l	heat-source length, reference length, m
p	local pressure, Nm^{-2}
p_B, q_B, r_B	components along the x_B, y_B, z_B axes, respectively, of the total angular velocity of the body axes relative to inertial space, deg sec^{-1}
$\dot{q}$	local-heat-transfer rate, Wm^{-2}
R	sphere radius, m
r	radius at the rear of heat source, m
S	reference area, wl, m^2

s	distance along heat-source surface measured from center of flat face (fig. 12), m
t	time, sec
u_B, v_B, w_B	components of flight velocity along x_B, y_B, z_B axes, respectively (fig. 2), m sec^{-1}
V	flight velocity, m sec^{-1}
w	heat-source width, m
x_B, y_B, z_B	body-fixed axes, origin at center of gravity, x_B coincident with a longitudinal axis of body (fig. 2)
x_B, y, z	aerodynamic axes, origin at center of gravity; x_B, z in the resultant angle-of-attack plane; y, z in the crossflow plane normal to the resultant angle-of-attack plane (fig. 13)
$\overline{z}_B$	center of gravity offset in the z_B direction from the geometric center of the heat source (fig. 1(a)), m
Γ	flight-path angle, measured negative below the local horizontal, deg
γ	ratio of specific heats, dimensionless
δ	magnitude of the dimensionless crossflow velocity vector in the aerodynamic axis system (fig. 13 and eq. (B1)), dimensionless
$\overline{\delta}$	flow deflection angle, deg
Θ	amplitude of roll oscillation measured from the value of ψ about which the heat source oscillates, deg
θ	oblique shock-wave angle, deg
θ_r	angular measure around a curved surface at the rear of the heat source, deg
$\dot{\lambda}$	angular rate at which the crossflow velocity vector rotates relative to a reference, nonrolling axis system whose y, z axes are in the crossflow plane, deg sec^{-1}
ρ	atmospheric mass density, kg m^{-3}
σ	resultant angle of attack defined by x_B axis and velocity vector (fig. 2), deg
ψ	angular measure of the z_B axis relative to the crossflow velocity vector (fig. 2), deg

Subscripts

A	maximum amplitude of oscillation
base	conditions in base-flow region of heat source
cyl	cylinder
e	conditions at outer edge of boundary layer
env	envelope of peak oscillations
equiv	equivalent-sphere value
I	inertial quantity
i	initial value or dummy index
j,k	dummy indices
max	maximum value
min	minimum value
$m1, m2$	locations on heat-source surface where one or more flow variables are matched
ref	reference-sphere value
s	stagnation-point value
sph	sphere
o	static aerodynamic quantity
1	conditions ahead of normal shock wave
2	conditions behind normal shock wave
*	sonic-point value

Superscript

$(\dot{})$	derivative with respect to time

SAFE ATMOSPHERE ENTRY OF AN ISOTOPE HEAT SOURCE WITH A SINGLE STABLE TRIM ATTITUDE AT HYPERSONIC SPEEDS

Lionel L. Levy, Jr.
Ames Research Center

and

Raymond K. Burns
Lewis Research Center

SUMMARY

A theoretical investigation has been made to design an isotope heat source capable of satisfying the conflicting thermal requirements of steady-state operation and atmosphere entry. The isotope heat source must transfer heat efficiently to a heat exchanger during normal operation with a power system in space, and in the event of a mission abort, it must survive the thermal environment of atmosphere entry and ground impact without releasing radioactive material. A successful design requires a compatible integration of the internal components of the heat source with the external aerodynamic shape. To this end, configurational, aerodynamic, motion, and thermal analyses were coupled and iterated during atmosphere entries at suborbital through superorbital velocities at very shallow and very steep entry angles.

Results indicate that both thermal requirements can be satisfied by a heat source which has a single stable aerodynamic orientation at hypersonic speeds. For such a design, the insulation material required to adequately protect the isotope fuel from entry heating need extend only half way around the fuel capsule on the aerodynamically stable (windward) side of the heat source. Thus, a low-thermal-resistance, conducting heat path is provided on the opposite side of the heat source through which heat can be transferred to an adjacent heat exchanger during normal operation without exceeding specified temperature limits.

INTRODUCTION

Present design concepts for isotope heat sources (IHS) are such that for some important space applications the thermal requirements for steady-state operation conflict with those for safe atmosphere entry (see ref. 1). A promising new concept to reduce this conflict was proposed in reference 2. The philosophy of the concept is that if a heat source can be designed with a single stable aerodynamic orientation, the insulation material required to protect the IHS from entry heating can be confined to 180° around the fuel capsule on the half that would be facing the oncoming flow. In addition to adequate thermal protection during entry, such a configuration provides a low-thermal-resistance, conducting heat path on the opposite side of the IHS through which heat can be transferred during steady-state operation without exceeding specified internal temperature limits.

The feasibility of this new concept was demonstrated in reference 2 for an IHS, called an Isoloaf, designed for use as the heat source for the Isotope Brayton Power System, a candidate power system for space stations. The results of preliminary analyses demonstrated satisfactory thermal performance during steady-state operation. The results also demonstrated that if the Isoloaf remains in the aerodynamically stable orientation throughout the entry heat pulse, the insulation material over only the aerodynamically stable side provides more than adequate thermal protection during entry at orbital velocity.

Subsequent to the publication of reference 2, calculations of the aerodynamic moment coefficients were made which indicate that the Isoloaf, with the dimensions and shape proposed, has two stable orientations ($\sigma = 90°$, $\psi = 0°$ and $\psi = 130°$). Unfortunately, one of these results in a rearward portion of the heat source (without insulation material) oriented forward throughout the entry heat pulse.

The present theoretical investigation was undertaken to (1) determine an aerodynamic shape for the Isoloaf that has a single preferred orientation at hypersonic speeds, and (2) to demonstrate its satisfactory thermal performance during both steady-state operation and atmosphere entry subsequent to various credible abort situations. The design approach employs a four-step iterative procedure: (1) assume an aerodynamic shape; (2) and (3) calculate pressure distributions and aerodynamic force and moment coefficients for all combinations of angle of attack and roll orientation; (4) analyze the Isoloaf motions indicated by six-degrees-of-freedom entry-trajectory calculations to determine that the heat source either attains (or oscillates about) the preferred orientation prior to peak heating or is in a continuously changing motion throughout the heat pulse such that no one portion of the heat source is exposed to the entry heating for an extended period of time. Two-dimensional temperature distributions through the Isoloaf were calculated to demonstrate that the temperatures of all heat-source components remained within limits specified for steady-state operation and atmosphere entry. The entry thermal analyses included the coupled effects of the time-dependent heat input, Isoloaf motion, and the concomitant changes in heating-rate distribution. The effects of ablation and possible shape changes on trajectory parameters, heat-source motion, heating-rate distribution, and material thermal response were not included, but should be in any final design analysis. The impact-intact survival of the Isoloaf is beyond the scope of the present study.

DESIGN AND THERMAL ANALYSIS

As noted earlier, a satisfactory Isoloaf configuration was sought by an iterative design procedure and its thermal performance was evaluated during steady-state operation and during atmosphere entry subsequent to various credible abort situations. In the interest of brevity, only the configuration that evolved as a result of the last iteration will be considered. This section summarizes the various inputs to the overall design procedure and thermal analysis. Details are included in appendices as noted.

Isoloaf Configuration

The shape, size, mass, and inertial properties of the Isoloaf are shown in figure 1. The external shape and center-of-gravity location are designed for the Isoloaf to fly with the flat side (0.188 m

by 0.089 m in fig. 1(a)) oriented forward. The fuel capsule and overall heat-source dimensions are identical to those given in reference 2. The layered arrangement of heat-source internal components is shown in figure 1(b). The isotope fuel, plutonium dioxide, is encased in refractory metals. The liner is a tantalum, 10-percent tungsten alloy, the strength member is a tantalum alloy (T-111), and the oxidation-resistant clad is a platinum, 20-percent rhodium alloy. The insulation material consists of three layers of pyrolytic graphite, and the external heat shield is made of POCO graphite. The physical and thermal properties of the separate heat-source components are listed in table 1. The gaps between adjacent components will be described later in connection with the thermal model. The mass and inertial properties are theoretical estimates.

Because the Isoloaf is a nonaxisymmetric body, two angles σ and ψ are used to describe its orientation relative to the flight velocity vector. As shown in figure 2, σ is the resultant angle of attack defined by the body longitudinal axis x_B and the flight velocity vector V (which also define the resultant angle-of-attack plane). The angle ψ in the crossflow plane, defined by the y_B z_B axes, is a measure of the roll orientation of the z_B axis from the crossflow velocity vector. All possible orientations of the Isoloaf are defined by the ranges $0° \leqslant \sigma \leqslant 180°$ and $-180° \leqslant \psi \leqslant 180°$.

Frequent reference will be made to several basic orientations. In the end-on attitude, $\sigma = 0°$ (or nearly so) and ψ is arbitrary. In the side-on attitude, $\sigma = 90°$ (or nearly so) for all values of ψ. End-on spinning and side-on spinning, of course, designate $\dot{\psi} \neq 0$. In pure pitch, $0° \leqslant \sigma \leqslant 180°$ and $\psi = 0°$ or $180°$. The preferred orientation, the side-on stable, flat-face-forward attitude, is defined as $\sigma = 90°$, $\psi = 0°$.

Pressure Distributions

Since the entry heat pulse occurs within the hypersonic speed range and since pressure distributions (as well as aerodynamic coefficients) are essentially independent of Mach number in this speed range, pressure distributions were calculated for a single set of flight conditions. The conditions were air in equilibrium at an altitude of 48.77 km and a velocity of 6.10 km/sec. These conditions were selected from point-mass trajectories as the average of those that exist near peak heating for the majority of entry conditions considered.

The pressure distributions were calculated for many orientations of the Isoloaf for $\sigma - \psi$ pairs over the ranges of $0° \leqslant \sigma \leqslant 90°$ and $0° \leqslant \psi \leqslant 180°$. Since the Isoloaf has two planes of mirror symmetry (x_B, z_B and y_B, z_B in fig. 2), these data are sufficient to define the pressure distributions (and aerodynamic coefficients) for all possible orientations. The aerodynamic symmetry relationships will be noted in connection with the aerodynamic coefficients.

Two procedures were used to calculate the pressure distributions, depending on the orientation of the Isoloaf. For most orientations, modified-Newtonian flow theory was used. For orientations in the neighborhood of the side-on attitude, the constant pressures over flat surfaces given by Newtonian theory yield moment coefficients that are not realistic for flow over blunt shapes with detached shock waves. Since proper moment coefficients are tantamount to attainment of the preferred Isoloaf orientation, a more realistic estimate of the pressure distributions at attitudes near the preferred orientation was deemed essential. In the side-on attitude ($\sigma = 90°, 0° \leqslant \psi \leqslant 180°$) the pressure distributions were calculated using a two-dimensional calculation procedure suggested by Kaattari (refs. 3-5). Pertinent details of the procedure are given in appendix A.

Aerodynamic Coefficients

The nonlinear aerodynamic moment system formulated in reference 6 was adopted for this study because it accurately describes the aerodynamic forces and moments for nonaxisymmetric bodies at large, as well as small, angles of attack. Accordingly, the aerodynamic force and moment coefficients are defined relative to the aerodynamic axis system of that reference. The coefficients in this axis system and the relationship between the aerodynamic and more commonly used body axis systems are noted in appendix B. The static aerodynamic coefficients were obtained by integrating the appropriate pressure distributions and the dynamic coefficients were calculated using the method of reference 7 (appendix B).

The key aerodynamic design feature that ensures the preferred Isoloaf attitude is that the center of gravity be offset in the $+z_B$ direction an amount equal to one-half the radius of the rearward-facing curved surfaces (fig. 1), and the radius must be equal to or greater than some minimum value. For $\sigma = 90°$ and $\bar{z}_B = 0.5r$, integrated Newtonian pressure distributions yield a single statically stable roll orientation at $\psi = 0°$ for $0 < r \leqslant 0.5w$. The configuration becomes more stable as r (at each rearward corner) increases from some small finite value to a single full radius. For $r = 0$ (a rectangular cross section), integrated pressure distributions obtained as indicated in appendix A yield statically stable roll orientations at $\psi = 0°$, 90°, and 180°. As r is increased toward $0.5w$ the configuration becomes neutrally stable at $\psi = 90°$ and 180° (not necessarily simultaneously) at some minimum value of r. The value of r_{min} depends on the flight conditions for which the pressure distributions are calculated and is not tractable in closed form. With further increases in r the neutrally stable points become unstable, and $\sigma = 90°$, $\psi = 0°$ remains the single preferred stable orientation. For the presently selected flight conditions $0.15w < r_{min} < 0.2w$. Effects on the important moment coefficients of design changes employing this offset-cg feature are noted in appendix B.

Six-Degrees-of-Freedom Trajectories

A six-degrees-of-freedom trajectory computer program was written especially for nonaxisymmetric bodies to obtain time histories of stagnation-point convective heat input and Isoloaf motions during atmosphere entry. The equations of motion and computer program described in reference 8 formed the basis for the present program. The equations of reference 8 for the aerodynamic forces and moments in the body axis system were rewritten to allow the aerodynamic coefficients to be input as functions of σ and ψ in the aerodynamic axis system and then transferred to the body axis system.

Three credible abort situations were considered: launch abort, orbital decay, and abort at superorbital velocity. Atmosphere entries subsequent to abort were initiated at suborbital through superorbital velocities (V_{I_i}) at very shallow and very steep entry angles (Γ_{I_i}). For each type of entry (V_{I_i} - Γ_{I_i} combination) various initial attitudes (σ_i, ψ_i) and initial angular velocities (p_{B_i}, q_{B_i}, and r_{B_i}) of the Isoloaf were considered. All entries were initiated in the equatorial plane at 121.92-km altitude heading due east into the 1962 Standard Atmosphere of a spherical, rotating earth. All entries were terminated in the hypersonic speed range after peak heating. Details of the selection of the abort situations and initial entry parameters are given in appendix C.

Of 21 entry trajectories calculated, seven were selected for thermal analysis as representative of the range of thermal environments the Isoloaf could credibly experience subsequent to the abort situations selected. A brief description of the seven entries (cases) and the initial entry parameters is given in table 2.

Thermal Model

To estimate the thermal response of the Isoloaf to the entry heating pulse, the heat source was simulated by the two-dimensional thermal model shown in figure 3. This matrix of nodes corresponds to one-half of the heat-source cross section. The groups of nodes associated with each of the heat-source components are indicated in the figure. The physical and thermal properties of each component have been noted in figure 1 and table 1.

The complete fuel capsule is simulated by nodes 1 through 36. Thermal generation of the fuel mass is simulated in nodes 1 through 12. All gaps between components within the fuel capsule (clad) were assumed to be 10 mils wide and helium filled.

The pyrolytic graphite insulation material (PG), extending half way around the capsule on the aerodynamically stable side of the heat source, is simulated by nodes 37 through 63 (fig. 3(b)). The POCO graphite heat-shield material (POCO) is simulated by the remaining nodes.

Two assumptions were used concerning the gaps between components that encase the fuel capsule. One assumption was that the gaps were evacuated and heat transfer is by radiation alone; the other was that the gaps were filled by air and heat transfer is by radiation and by conduction through continuum air. In all cases, the initial temperature distributions were taken to be the equilibrium temperature of the heat source in space with all gaps outside the clad evacuated.

The temperature of each node during steady-state operation and during atmosphere entry was determined using the CINDA-3G computer code of reference 9. This code calculates the heat exchange by conduction and/or radiation between all adjacent nodes. During steady-state operation, temperature distributions through the heat source were determined in response to the thermal generation in the fuel nodes and to the thermal radiation from appropriate exterior surface nodes to an adjacent heat exchanger (ref. 2). During atmosphere entry, temperature time histories for the nodal model were determined in response to the thermal generation in the fuel nodes and to the entry heating to, and thermal radiation from, the exterior surface nodes. The entry heating was applied to the exterior POCO nodes (113 to 124) using the heating-rate distributions and heat-input procedure noted below.

Heating-Rate Distributions

Calculation of the heating-rate distributions for all possible orientations of the Isoloaf is beyond the scope of this investigation. Fortunately, however, the Isoloaf is designed to fly in (or oscillate about) the preferred orientation during most of the entry heat pulse. Therefore, for purposes of calculating the heating-rate distributions and performing the thermal analyses, the Isoloaf was assumed to fly in the side-on attitude ($\sigma = 90°$) throughout the entry and only roll orientations in ψ were considered. Thus, consistent with earlier assumptions of two-dimensional

flow for calculation of the pressure distributions for the side-on attitude and a two-dimensional thermal model, two-dimensional calculation methods were employed to obtain the heating-rate distributions. These assumptions will result in conservative (high) estimates of the temperature distributions through the Isoloaf since, during periods of oscillatory motion for which $\sigma = 90° \pm \Delta\sigma$, with $\Delta\sigma$ large, the heat-source end regions (which are well insulated from the capsule) actually receive the highest heating rates rather than the central regions represented by the thermal model employed.

The heating-rate distributions were calculated by two methods, depending on the nature of the bow shock wave associated with a particular ψ orientation of the Isoloaf. For roll orientations for which the bow shock wave is detached from the Isoloaf (most values of ψ), the heating-rate distributions were calculated using the method of reference 10. These results were referenced to the stagnation-point heating rate of a 0.3048-m-radius sphere as described in appendix D. For roll orientations for which the shock wave was attached to a corner of the Isoloaf, the heating-rate distributions were calculated using the method of reference 11. These results, for a cone, were corrected for flow over a wedge and also referenced to the stagnation-point heating rate of the reference sphere (see appendix D).

Entry Heat Input

The heat input to each exterior surface node during entry was determined by coupling the heating-rate distributions with time histories of the Isoloaf orientation and reference heating rate. To facilitate this process, the heating-rate distributions for each value of ψ were averaged, as indicated in appendix E, over each *ith* exterior node to obtain the nodal heating factors $F_i(\psi)$.

For many time intervals during most of the entries considered, the rate of change of heat source orientation was significantly higher than the rate of change of the reference heating rate. For these periods, the heating factors were time averaged to simulate the variation in each nodal heating factor with heat source motion. This averaging procedure for obtaining time histories of the entry heating input to each exterior node is also described in appendix E.

RESULTS AND DISCUSSION

In a viable IHS design, the internal components and the external aerodynamic shape are integrated such that during steady-state power-system operation the temperatures of components inside the fuel capsule do not exceed a specified limit, and during atmosphere entry the temperature of the outside case of the fuel capsule does not exceed another specified limit. During steady-state operation the maximum allowable temperature is determined by the compatibility of the fuel with the fuel liner. The upper limit assumed for this study is 1478°K (refs. 1 and 2). During entry the oxidation-resistant clad must not reach its melting temperature (2145°K, see table 1).

The following paragraphs examine results of the present analyses to demonstrate that the Isoloaf does satisfy the two thermal requirements. The launch abort entry (case 1, table 2) is examined in detail. A few unusual motions of the Isoloaf occurred during some entries but did

not degrade the thermal performance; these are noted and the motion (at peak heating) and thermal results for other entries are summarized.

Trajectory and Motion Results

Time histories of the reference heating rate $\dot{q}_{s,ref}$ and the maximum amplitude of the roll oscillation Θ_A during entry from a launch abort, case 1, are shown in figures 4 and 5, respectively. As noted earlier, all entries were terminated in the hypersonic speed range after peak heating. In figure 5, note that following arrest of the spinning ($\Theta_A = 180°$), the oscillations (about $\psi = 0°$ in this case) decreased (damped) until about 88 sec into the entry, then increased slightly and appear to start to damp again. The increase in Θ_A occurs as the dynamic pressure begins to decrease. Also shown in figure 5 is the step-function approximation $\Theta_A(\Delta t)$ used in determining the heating-rate distribution during entry (see appendix E). The use of smaller steps should have a negligible effect on the results of the thermal analysis. The maximum amplitude of oscillation in σ about the side-on attitude was less than ±3° and therefore is not shown. Of primary concern is the motion of the Isoloaf relative to the occurrence of peak heating. The tendency of the oscillatory motion about the preferred orientation to damp prior to peak heating is shown in figure 6. A value of the ordinate of one indicates continuous spin; a value of zero indicates the attainment of the preferred stable orientation with no motion. The dashed portion of the curve indicates the oscillatory motion subsequent to peak heating.

Different combinations of initial trajectory and motion parameters, of course, result in different heat-source motions relative to peak heating. Figure 7 gives an example (not listed in table 2) of the great variety of motions a heat source can experience. The Isoloaf motion relative to peak heating is shown superimposed on the altitude time history for a superorbital entry normal to the earth's surface. The entry was initiated with the Isoloaf spinning in the end-on attitude. By the time the heating rate reached 5 percent of its maximum value (3.3 sec), the Isoloaf had pulled up into a coning and oscillatory motion making large excursions in both σ and ψ about the preferred orientation. This motion quickly damped (more so in ψ) prior to $0.5\dot{q}_{s,ref,max}$ (6.75 sec) and at $\dot{q}_{s,ref,max}$ (8.25 sec) became essentially a pitching motion with small oscillations in ψ (i.e., $\sigma = 90° \pm 45°$ and $\psi = \pm 17°$). A second later at $0.5\dot{q}_{s,ref,max}$, $\sigma = 90° \pm 40°$ and $\psi = \pm 10°$.

Several interesting motions occurred briefly during some of the entries. For the entry subsequent to launch abort with the heat source spinning in the end-on attitude (case 2, table 2), the Isoloaf experienced a coning motion during which the uninsulated side ($\psi = 180°$) was exposed to the free stream for a period of 12 sec. During this period, the maximum coning angle (angle of attack) increased from 6° to 45°. Fortunately, this occurred early in the entry when the heating rate was low ($0.1 < \dot{q}/\dot{q}_{s,ref,max} < 0.29$). The same type of heat-shield-rearward motion occurred for about 11 sec early in a shallow, superorbital entry ($\Gamma_{I_i} = -10°$) with the Isoloaf initially spinning end-on. In this case, the heating rate was less than $0.27\ \dot{q}_{s,ref,max}$. As can be seen in figure 7, this type of motion did not occur during the steep, superorbital entry with the Isoloaf initially spinning end-on. During orbital decay with the heat source initially end-on and tumbling (case 5), the Isoloaf experienced a transition from a tumbling to a propeller-like motion with one side ($\psi = 86°$) exposed to the free stream until the heating rate reached $0.5\ \dot{q}_{s,ref,max}$. Angular variations at the outset were $5° \leqslant \psi \leqslant 175°$ and $0° \leqslant \sigma \leqslant 180°$ and at the end of this period the propeller-like motion had damped such that $78° \leqslant \psi \leqslant 94°$ and $85° \leqslant \sigma \leqslant 95°$. (Subsequent oscillations in ψ occurred about $\psi = 0°$.) Even though an uninsulated

region of the Isoloaf was exposed to the flow during most of this portion of the heat pulse, as will be seen later, there were no deleterious effects on the thermal performance of the heat source.

For all 21 entries examined, the Isoloaf attained an oscillatory motion (in both σ and ψ) about the preferred orientation prior to peak heating or was continuously coning and spinning so that no one portion of the Isoloaf was exposed to the flow for an extended period of time. The amplitudes of oscillation in σ and ψ at peak heating during the entries listed in table 2 are representative of all 21 entries, and the σ - ψ motions at peak heating and values of $\dot{q}_{s,ref,max}$ are given in table 3.

Thermal Results

Steady-state operation– The conducting heat paths and gaps of the present Isoloaf design are quite similar to the original design considered in reference 2 (full radius at the rear) as the heat source for the Isotope Brayton Power System. Therefore, for this type of power-system application, the results of the thermal analysis of the original design during steady-state operation are considered to apply equally well to the present configuration. In reference 2 the back surface was found to furnish a temperature of 1290°K to the adjacent heat exchanger, and the fuel-liner hot-spot temperature did not reach the limiting value of 1478°K; in fact, the fuel hot-spot temperature was also less than 1478°K.

Entry– Time histories of some of the key heat-source temperatures during entry case 1 (table 2) are given in figures 8 through 10. The POCO graphite external surface temperatures at five locations around the Isoloaf are shown in figure 8. As shown in figure 5, the Isoloaf remained spinning for about 50 sec and then began oscillating with the flat, insulated side forward (about $\psi = 0°$). These motions directly influence the variations in external temperature shown in figure 8. The temperatures varied rather uniformly during the spinning motion. When the heat source began oscillating about the flat side, the temperatures of that surface (nodes 113 and 115) increased much more rapidly than those on the other sides. The temperature on the trailing side (node 124) decreased slightly after spinning was arrested; consequently the heating rate was reduced, but rose again as the reference heat pulse continued to increase.

The temperatures of prime interest for this heat source are those of the oxidation-resistant clad on the capsule, which must be kept below its melting temperature (2145°K). The temperatures of the graphite surfaces adjacent to the clad also are of prime interest, since they represent the maximum temperature the clad could reach in the event physical contact occurs during entry. These temperatures, at three circumferential locations, are given for case 1 in figures 9 and 10. For the results in figure 9, it was assumed that all gaps between materials exterior to the capsule clad remained evacuated throughout the entry heat pulse, and for figure 10 it was assumed that these gaps became air filled at the beginning of entry.

A comparison of the initial temperatures in figures 9(a) and (b) shows that the temperature difference between the clad and the adjacent surfaces are greatest on the uninsulated sides, indicating that in equilibrium most of the energy is emitted from these sides of the heat source. As the Isoloaf enters, the direction of heat transfer is reversed, and the adjacent surfaces become hotter than the clad. The effectiveness of the pyrolytic graphite insulation is clearly demonstrated by

the fact that the clad node 31 and the adjacent PG node 37 were affected least by entry heating even though the POCO on that side of the heat source was the hottest (see nodes 113 and 115, fig. 8). The hottest point on the clad was at the side of the Isoloaf near the end of the insulation (node 34). This results from a combination of heat conduction through the POCO from hotter regions to node 64 and from entry heating to the side of the heat source (such as to node 119).

In figure 10, where the gaps between entry protection materials were assumed to be filled with air, the temperatures around the clad and the adjacent graphite surfaces showed slightly more response than for the evacuated gaps. Due to the lower thermal resistance of the gaps, the peak temperatures were slightly higher than in the vacuum-gap case, but remained well below the clad melt temperature. The initial decrease in temperature in figure 10 is due to a readjustment from the initial temperature distribution, which assumed vacuum gaps between entry protection materials.

The peak temperatures reached by the clad and the surface adjacent to it at three locations around the fuel capsule are given in table 4 for the seven cases for which entry thermal analyses were made. These results are for the assumption of air-filled gaps, since the clad temperatures were slightly higher with this assumption than with the assumption of evacuated gaps. All the clad temperatures listed are well below the clad melt temperature (2145°K). Furthermore, the highest temperature reached by an adjacent surface was less than 90 percent of the maximum allowable temperature. This occurred on the side of the heat source during superorbital entry with the Isoloaf initially spinning side-on (node 64, case 6).

Even though all entries were terminated after the occurrence of peak heating, the temperatures of some of the nodes did not reach a peak during the time interval considered but continued to rise as a result of heat transfer from hotter portions of the heat source. An example of this behavior is illustrated in figures 9 and 10 for nodes 31 and 37. From these data it is obvious that had the time interval of the analysis been extended, the continued temperature rise expected for these nodes would not have been large. In such cases, the temperature reached at the termination of the entry calculations is listed in table 4 and denoted by an asterisk.

For entries with the Isoloaf initially side-on stable (no spin, cases 3 and 7), the heat source remained essentially side-on with the insulated side forward throughout the trajectory. The temperature results show that the insulation, surrounding only the aerodynamically stable side of the capsule, more than adequately protects the entire capsule. The addition of an initial spin about the side-on attitude (arrest and subsequent oscillation) results in a distribution of generally higher temperatures through the Isoloaf. This can be seen by comparing the temperatures for cases 3 and 7 with those for cases 1 and 6. Although the amplitude of oscillation near peak heating was large enough to expose the uninsulated sides of the heat source to significant heating ($\Theta_A \approx 83°$ for case 1 and $\Theta_A \approx 55°$ for case 6, see table 3), the capsule temperature remained well within limits.

For launch-abort case 2 the Isoloaf was initially spinning in the end-on attitude ($\sigma = 0°$) and the angle σ varied considerably throughout the trajectory. As explained previously, the two-dimensional thermal model is strictly valid only when the heat source remains side-on ($\sigma = 90°$). Even though this thermal model yields conservatively high temperatures for case 2, the results are included in table 4 because, in addition to large variations in σ, the heat source also oscillated about the uninsulated side (heat shield rearward with $\psi = 180°$) for a short period (~ 12 sec) early

in the trajectory. A comparison of the temperatures for case 2 with those for launch-abort entries with the Isoloaf in the side-on attitude (cases 1 and 3) indicates that the brief period of oscillations heat shield rearward did not seriously degrade the entry thermal performance of the heat source. It is emphasized that the higher temperatures of case 2 (compared to cases 1 and 3) are due, in part, to the conservative assumption that $\sigma = 90°$ throughout the entry and the use of a two-dimensional thermal model. The same is true of the results for the orbital-decay case 4 compared with those for case 5 (tables 3 and 4).

CONCLUDING REMARKS

A theoretical investigation has been made to design an isotope heat source capable of satisfying the conflicting thermal requirements of steady-state operation and atmosphere entry. That is, the heat source must be able to transfer heat efficiently to a heat exchanger during normal operation with a power system in space and, in the event of a mission abort, it must be able to survive the thermal environment of atmosphere entry without the release of radioactive material. A successful design requires a compatible integration of the internal components of the heat source with the external aerodynamic shape. For this purpose, aerodynamic force and moment coefficients were calculated from two- and three-dimensional pressure distributions over candidate heat-source shapes for all possible flight orientations. Six-degrees-of-freedom trajectory calculations were made to determine the heating rate and heat-source motion during atmosphere entries from suborbital through superorbital velocities at very shallow and very steep entry angles with various initial heat-source motions. Two-dimensional heating-rate distributions were calculated for use in two-dimensional thermal analyses made for some of these entries. These analyses included the combined effects of time-dependent heat inputs and heat-source motions, and motion-dependent heating-rate distributions. Also, the thermal performance of the heat source was estimated during steady-state operation with a particular space power system.

Results of the investigation indicate that both thermal requirements can be satisfied by a heat source, called an Isoloaf, which has a single stable aerodynamic orientation at hypersonic speeds. For such a design, the insulation material required to adequately protect the isotope fuel from entry heating need extend only halfway around the fuel capsule on the aerodynamically stable side of the heat source. Thus, a low-thermal-resistance, conducting heat path is provided on the opposite side of the Isoloaf through which heat can be transferred to an adjacent heat exchanger during normal operation without exceeding specified temperature limits. This was demonstrated in an earlier application of the Isoloaf concept to the Isotope Brayton Power System. The present Isoloaf configuration was found to attain a satisfactory motion history during passage through the entry heat pulse for all entries examined, and the results of the thermal analyses indicate that the insulation on only the aerodynamically stable side provides more than adequate protection, even though during the early part of some entries the uninsulated side of the Isoloaf was exposed to the free stream for short periods of time. In the worst case, the highest temperature reached by any critical internal component was found to be less than 90 percent of the limiting value, the melting temperature of the outside case of the fuel capsule.

Ames Research Center
National Aeronautics and Space Administration
Moffett Field, Calif., 94035, March 22, 1972

APPENDIX A

PRESSURE-DISTRIBUTION CALCULATIONS FOR ISOLOAF IN THE SIDE-ON ATTITUDE ($\sigma = 90°$, $0° \leqslant \psi \leqslant 180°$)

The calculation procedure suggested by Kaattari (refs. 3–5) involves two basic assumptions: (1) the Mach number is sufficiently high that asymptotic forms of the gas–dynamic equations in reference 12 can be used, and (2) two–dimensional flow of an ideal gas with specific–heat ratio γ equal to that of the air in equilibrium. Invoking assumption (1)

$$\gamma = \frac{(\rho_2/\rho_1) + 1}{(\rho_2/\rho_1) - 1} \tag{A1}$$

and the stagnation–point pressure coefficient is given by

$$C_{p_S} = 2\left[1-\left(\frac{\rho_2}{\rho_1}\right)^{-1}\right] \tag{A2}$$

The normal–shock density ratio ρ_2/ρ_1 may be obtained from reference 13 as a function of flight conditions. For the present conditions $\rho_2/\rho_1 = 13.7$, $\gamma = 1.157$, and $C_{p_S} = 1.854$.

The procedure utilizes different calculation methods over various segments of that portion of the configuration exposed to the oncoming flow. A sample flow–field model is shown in figure 11 for $\sigma = 90°$ and $\psi = 20°$. Between the sonic points, the shock shape, shock standoff distance, and stagnation–point velocity gradient are obtained for $\psi = 0°$ using the method of reference 3. The method of reference 4 is used to correct these quantities for the desired value of ψ and to relocate the stagnation point. The pressure gradients at the sonic points are obtained as indicated in reference 5, and the method of that reference is used to calculate the pressure distribution between the stagnation point and sonic point, in both directions, utilizing the known flow properties at the end points. (Kaattari developed this procedure for combining his methods of refs. 3–5). At the rightmost sonic point in figure 11 (looking downstream), the flow is assumed to separate such that the base pressure equals free–stream static pressure ($p_{base} = 0.00225\ p_S$). The flow is assumed to expand around the leftmost corner to a value of the pressure that would exist behind a shock wave attached to a two–dimensional wedge (see sketch (a)). The flow–deflection angle $\bar{\delta}$ for the sample case shown in figure 11 is 20°. The surface pressure coefficient obtained from reference 12 and assumption (1) is

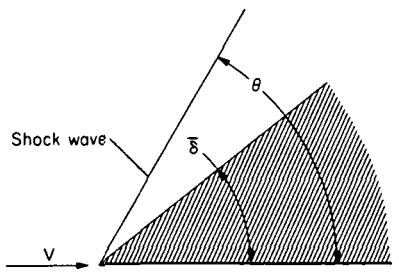

Sketch (a)

$$C_p = 2\left[1-\left(\frac{\rho_2}{\rho_1}\right)^{-1}\right]\sin^2\theta \tag{A3}$$

where the oblique shock angle θ is evaluated from

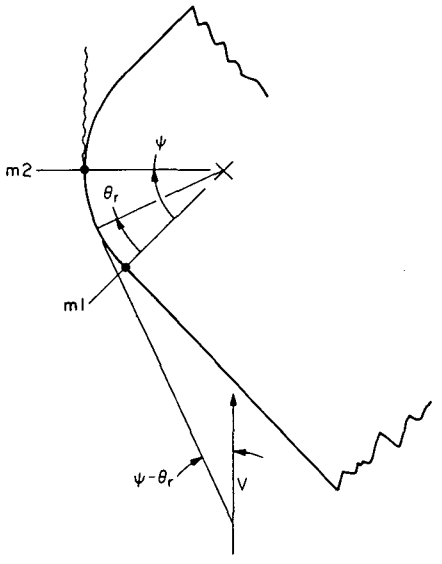

Sketch (b)

$$\bar{\delta} = \theta - \tan^{-1}\left[\left(\frac{\rho_2}{\rho_1}\right)^{-1}\tan\theta\right] \tag{A4}$$

The pressure coefficient is assumed constant along the side of the body from the corner to the point of tangency with the curved surface facing the free stream (point $m1$ in sketch (b)). From this point the flow is assumed to expand around the curved surface, with a Newtonian-type variation, to free-stream static pressure at a point where the local surface slope is parallel to the free-stream direction. This is at $m2$ in sketch (b), at which point the flow is assumed to separate. The expression that forces the desired variation in C_p to match the values at the end points ($m1$ and $m2$) is

$$C_p(\theta_r) = C_{p_s}\sin^2\left[\left(\frac{\psi-\theta_r}{\psi-\theta_{m1}}\right)M1 + \left(\frac{\theta_r-\theta_{m1}}{\psi-\theta_{m1}}\right)M2\right], \quad \theta_{m1} \leqslant \theta_r \leqslant \theta_{m2} \tag{A5}$$

where

$$Mn = \sin^{-1}\left(\frac{C_{p_{mn}}}{C_{p_s}}\right)^{1/2}, \quad n = 1, 2 \tag{A6}$$

For the sample flow field shown in figure 11 the value of $C_{p_{m1}}$ is obtained from equations (A3) and (A4) for $\bar{\delta} = 20°$; $C_{p_{m2}} = C_{p_{base}} = 0$, $\theta_{m1} = 0°$, and $\theta_{m2} = 20°$. The pressure-coefficient distribution for this case is shown in figure 12. The pressure coefficient normalized by the stagnation-point value is shown as a function of distance along the body surface s measured from the center of the flat face and normalized by the Isoloaf half width.

For other values of ψ, the location of some combination (two or more) of the stagnation point, sonic points, and the pressure matching points ($m1$ and $m2$) on the curved surface(s) will change. However, the pressure coefficient can be calculated over each segment of the surface by one of the three methods just described. For example, for $59.8° < \psi \leqslant 90°$, the rightmost sonic point is located at the corner $2s/w = -1$ and the other is on the upstream curved surface at a location θ_{r_*}. The variation in C_p around the remaining portion of the curved surface is given by equations (A5) and (A6) where now $C_{p_{m1}} = C_{p_*}$, $C_{p_{m2}} = 0$, $\theta_{m1} = \theta_{r_*}$, and $\theta_{m2} = \psi$.

As indicated in reference 12, a two-dimensional wedge can support an attached shock wave for values of $\overline{\delta}$ less than $\sin^{-1}(1/\gamma)$. Thus, for the present conditions, the flow is attached to the corner $2s/w = -1$ for $30.2° < \psi < 59.8°$. For this range of ψ, C_p on the sides of the Isoloaf is obtained from equations (A3) and (A4), where $\overline{\delta} = 90° - \psi$ for $-1 \leqslant 2s/w \leqslant 1$ and $\overline{\delta} = \psi$ for $-2.914 \leqslant 2s/w \leqslant -1$ (-2.914 is the point of tangency noted in fig. 11).

Pressure distributions for the Isoloaf in pure pitch ($0° \leqslant \sigma \leqslant 90°$, $\psi = 0°$ or $180°$) were also calculated using the procedure just described. Although the flow field cannot justifiably be considered two-dimensional for these orientations, the pressure distributions so obtained are believed more realistic than those predicted by Newtonian theory.

APPENDIX B

AERODYNAMIC COEFFICIENTS AND AXIS SYSTEMS

The aerodynamic force and moment coefficients are defined relative to the aerodynamic axis system of reference 6. A vector representation of the coefficients in this axis system and the relationship between the aerodynamic and body axis systems are shown in figure 13. The two axis systems have a common origin at the center of gravity and a common x_B axis. The aerodynamic axes y, z are in the crossflow plane, rotated through the angle ψ, such that the z axis is alined with the crossflow velocity vector. In terms of the dimensionless quantities in figure 13, the magnitude of this vector is

$$\delta = \left[\left(\frac{v_B}{V}\right)^2 + \left(\frac{w_B}{V}\right)^2\right]^{1/2} = \sin\sigma \tag{B1}$$

Coefficients C_A, C_N, and C_Y are the axial-, normal-, and side-force coefficients, respectively; C_l, C_m and C_n are the rolling-, pitching-, and side-moment coefficients, respectively. Detailed expressions for the coefficients used in the present study are (ref. 6):

$$\left.\begin{aligned}
C_A(\sigma,\psi) &= C_{A_o}(\sigma,\psi) \\
C_N(\sigma,\psi) &= C_{N_o}(\sigma,\psi) \\
C_Y(\sigma,\psi) &= C_{Y_o}(\sigma,\psi) \\
C_l(\sigma,\psi) &= C_{l_o}(\sigma,\psi) \\
C_m(\sigma,\psi) &= C_{m_o}(\sigma,\psi) + \frac{\dot{\sigma}l}{V} C_{m_{\dot{\sigma}}}(\sigma,\psi) + \frac{\dot{\lambda}l}{V}\tan\sigma\,\frac{C_{m_{\dot{\phi}}}(\sigma,\psi)}{\delta} \\
C_n(\sigma,\psi) &= C_{n_o}(\sigma,\psi) + \frac{\dot{\sigma}l}{V} C_{n_{\dot{\sigma}}}(\sigma,\psi) + \frac{\dot{\lambda}l}{V}\tan\sigma\,\frac{C_{n_{\dot{\phi}}}(\sigma,\psi)}{\delta}
\end{aligned}\right\} \tag{B2}$$

The reference area and length for the coefficients are $S = wl$ and l, respectively. The subscript o denotes static aerodynamic coefficients. The dynamic coefficients $C_{m_{\dot{\sigma}}}$ and $C_{n_{\dot{\sigma}}}$ are contributions to the pitching- and side-moment coefficients, respectively, due to planar pitching oscillations (about a fixed σ) in the resultant angle-of-attack plane with ψ = constant. Similarly, $C_{m_{\dot{\phi}}}$ and $C_{n_{\dot{\phi}}}$ are contributions due to steady coning motion at constant σ and ψ. As noted in reference 6, $\dot{\lambda}$ is the angular rate at which the crossflow velocity vector rotates relative to a reference, nonrolling axis system whose y, z axes are in the crossflow plane. The aerodynamic coefficients are mutually

transferable between the aerodynamic and body axis systems. For example, the moment system is transferable through the relations

$$\left.\begin{aligned} C_l &= C_{l_B} \\ C_m + iC_n &= e^{i\psi}\left(C_{m_B} + iC_{n_B}\right) \end{aligned}\right\} \tag{B3}$$

The compatible forms for the transferred terms (static and dynamic) are given in reference 6.

Values of the static aerodynamic coefficients in pure pitch ($0° \leqslant \sigma \leqslant 90°$, $\psi = 0°$) and in the side-on attitude ($\sigma = 90°$, $0° \leqslant \psi \leqslant 180°$) were obtained by integrating the appropriate pressure distributions with respect to the aerodynamic axes. The dynamic coefficients for these $\sigma-\psi$ orientations, as well as the static and dynamic coefficients for all other orientations, were obtained using modified Newtonian pressure distributions in the method of reference 7. In reference 7 the coefficients are referred to the body-axis system and, therefore, were transferred to the aerodynamic axis system.

The aerodynamic coefficients calculated for various $\sigma-\psi$ pairs for $0° \leqslant \sigma \leqslant 90°$ and $0° \leqslant \psi \leqslant 180°$ are listed in table 5. In view of the two planes of mirror symmetry noted earlier, these data are sufficient to define the coefficients for all possible orientations of the Isoloaf. The symmetry relationships are given in table 6.

The aerodynamic requirements for a single stable trim orientation for the Isoloaf in the side-on, flat-face-forward attitude are that the conditions

$$\left.\begin{aligned} & C_{m_o}(\sigma,\psi) = 0 \\ & \left.\frac{\partial C_{m_o}(\sigma,\psi)}{\partial \sigma}\right|_{\sigma = const} < 0 \\ & C_{l_o}(\sigma,\psi) = 0 \\ & \left.\frac{\partial C_{l_o}(\sigma,\psi)}{\partial \psi}\right|_{\psi = const} < 0 \end{aligned}\right\} \tag{B4}$$

be satisfied simultaneously for $\sigma = 90°$ and $\psi = 0°$, and for no other $\sigma-\psi$ pair. The moment coefficients in figure 14 clearly demonstrate that for angular displacements in the two planes of mirror symmetry all of conditions (B4) are satisfied at $\sigma = 90°$ and $\psi = 0°$. Detailed examination of the data in table 5 revealed that at least two of conditions (B4) are violated for all other $\sigma-\psi$ pairs. The "waviness" in C_{l_o} (90°, ψ) in the neighborhood of $\psi = 30°$ and 60° (fig. 14(b)) is a result of fairing through discontinuities in the data associated with the attachment of shock waves to the sharp edges of the Isoloaf in the angle range $30.2° \leqslant \psi \leqslant 59.8°$. Similarly, the pitching-moment data in figure 14(a) have been faired near $\sigma = 30°$, 60°, 120°, and 150°.

As noted earlier, the key design feature that ensures the preferred Isoloaf attitude is that the center of gravity be offset in the $+z_B$ direction an amount equal to one-half the radius of the rearward-facing curved surfaces (see fig. 1) and $r \geq r_{min}$. This is particularly pertinent to satisfying the requirements on the rolling moment coefficient given in conditions (B4). Furthermore, the larger the value of r, the more favorable the C_{l_0} $(90°, \psi)$ data, the limiting case being a single, full radius at the rear, $r = 0.5w$. The value of r for the present Isoloaf design is the largest value greater than r_{min} ($r_{min} < 0.2w$) consistent with the overall dimensions selected, and with the relation $\bar{z}_B = 0.5r$, which permits sufficient thicknesses of insulation and heat-shield material to ensure safe atmosphere entry. The improvement in C_{l_0} $(90°, \psi)$ over the present design that could be expected from an Isoloaf with $r = 0.5w$ and $\bar{z}_B = 0.5r$ can be seen in figure 15. Such a design, of course, would require a different size or type of fuel cell and/or different overall heat-source dimensions. Similar improvements in C_{m_0} $(\sigma, 0°)$ are simultaneously realized as $\bar{z}_B$ increases.

APPENDIX C

ABORT SITUATIONS AND INITIAL ENTRY PARAMETERS

Three credible abort situations were considered: launch abort, orbital decay, and abort at superorbital velocity. All entries subsequent to abort were assumed to begin at an altitude of 121.92 km.

Launch abort was assumed possible at any point along a nominal launch trajectory following a short (less than 25 sec) uncontrolled burn of the booster, or misalinement of one or more engines. Subsequent entries occur for a variety of initial velocities and flight-path angles. The particular combination of these trajectory parameters selected for this study was that which resulted in the greatest total convective heat absorbed during entry – that is, an initial inertial velocity V_{I_i} of 7.62 km/sec and an initial inertial flight-path angle Γ_{I_i} of -7.7°.

Orbital decay, of course, could be a normal or an abnormal entry. The assumed initial trajectory parameters were V_{I_i} = 7.83 km/sec and Γ_{I_i} = -0.02°.

An example of a credible abort at superorbital velocity is propellant depletion just prior to attaining earth-escape velocity and transfer to a transplanetary trajectory. Though such an abort can result in multiple-pass entries, only single-pass entries were considered. Initial trajectory parameters of V_{I_i} = 10.97 km/sec and Γ_{I_i} = -10° were selected as representative of a severe thermal environment without subjecting the Isoloaf to excessive deceleration loads (less than 45 g in this case). Although the Isoloaf would probably fail from thermal shock, or certainly fail from the deceleration loads, which can exceed 400 g for entries straight into the earth's atmosphere (Γ_{I_i} = -89.9°) at 10.97 km/sec, such entries were examined for their academic interest (see fig. 7), particularly the likely Isoloaf motion relative to the occurrence of peak heating.

Conditions defining various initial attitudes and angular velocities of the Isoloaf were also considered for each type of entry just described. These conditions ranged from the preferred orientation with no angular velocity, through orientations with angular velocities that initially produce tumbling and/or spinning motions, to spinning in the end-on attitude at a feasible estimated maximum rate. The maximum initial angular velocity imparted to the Isoloaf was estimated to be 400°/sec as a result of a launch abort in which the uncontrolled burn noted earlier occurred with all engines "hard over."

APPENDIX D

HEATING-RATE-DISTRIBUTION CALCULATIONS FOR ISOLOAF IN THE SIDE-ON ATTITUDE ($\sigma = 90°$, $0° \leqslant \psi \leqslant 180°$)

Heating-rate distributions were calculated by either of two methods, depending on the nature of the bow shock wave associated with each particular roll orientation of the Isoloaf. For roll orientations for which the bow shock wave is detached from the Isoloaf (most values of ψ), the following expression was used to obtain dimensionless heating-rate distributions:

$$\frac{\dot{q}[\psi,(2s/w)]}{\dot{q}_{s,ref}} = \frac{\dot{q}[\psi,(2s/w)]}{\dot{q}_s(\psi)} \frac{\dot{q}_s(\psi)}{\dot{q}_s(0)} \frac{\dot{q}_s(0)}{\dot{q}_{s,cyl}} \frac{\dot{q}_{s,cyl}}{\dot{q}_{s,sph}} \frac{\dot{q}_{s,sph}}{\dot{q}_{s,ref}} K(\psi) \tag{D1}$$

The first ratio in equation (D1) is the cold-wall, laminar convective heating-rate distribution for any value of ψ normalized by the heating rate to the stagnation point for that roll orientation. A computer program written for the method of reference 10, a method based on laminar boundary-layer theory for a swept cylinder, was used to calculate these distributions. The method requires a knowledge of the distributions of surface pressure and velocity and velocity gradient at the outer edge of the boundary layer. The pressure distributions and stagnation-point velocity gradients were obtained from the calculations noted in appendix A. The velocity distributions were calculated from the pressure distributions as indicated in reference 10, and the velocity gradients were obtained from a computer routine for smoothing and differentiating. A special smoothing routine was included in the program to ensure a consistent set of input data (pressure, velocity, and velocity gradient) for all values of $2s/w$, particularly at the stagnation point and at values where the pressures were discontinuous (fig. 12).

The next four ratios in equation (D1) are used to relate the heating-rate distribution for any ψ to the stagnation-point value of the reference sphere. The second ratio relates stagnation-point heating for any ψ to that for $\psi = 0°$, flat face forward, and equals the ratio of stagnation-point velocity gradients

$$\frac{\dot{q}_s(\psi)}{\dot{q}_s(0)} = \frac{[d(V_e/V)/d(2s/w)]_s(\psi)}{[d(V_e/V)/d(2s/w)]_s(0)} \tag{D2}$$

Values for the stagnation-point velocity gradients are given in table 7 as a function of ψ. The next ratio $\dot{q}_s(0)/\dot{q}_{s,cyl}$ accounts for the difference in stagnation-point velocity gradients between a flat plate and a cylinder normal to the free stream. The value 0.6 was obtained from the computer program described in reference 14. The ratio $\dot{q}_{s,cyl}/\dot{q}_{s,sph}$ accounts for the difference in stagnation-point heating rates for a cylinder and a sphere of the same radius (an equivalent radius for the Isoloaf, $R_{equiv} = w/2$). The value $1/\sqrt{2}$ was used (ref. 15). The last ratio relates the stagnation-point heating rate of the equivalent sphere to that of the reference sphere, as follows:

$$\frac{\dot{q}_{s,sph}}{\dot{q}_{s,ref}} = \left(\frac{R_{ref}}{R_{equiv}}\right)^{1/2} = \left[\frac{R_{ref}}{(w/2)}\right]^{1/2} \tag{D3}$$

Thus, the product of the five ratios in equation (D1) yields a two-dimensional, dimensionless heating-rate distribution.

Finally, to obtain heating-rate distributions more representative of a three-dimensional configuration, the correction factor $K(\psi)$ for a general three-dimensional stagnation point was included in equation (D1). This factor was evaluated as indicated in reference 16 and for the Isoloaf can be shown to be

$$K(\psi) = \left\{1 + \left(\frac{w}{l}\right) \frac{[d(V_e/V)/d(2s/w)]_s\,(0)}{[d(V_e/V)/d(2s/w)]_s\,(\psi)}\right\}^{1/2} \tag{D4}$$

The heating-rate distribution for the sample flow field and pressure-coefficient distribution shown in figures 11 and 12, respectively, is shown in figure 16. The locations of the POCO exterior-surface nodes are indicated for reference.

Some indication of the accuracy of the heating rates calculated by the above procedure was obtained by comparing the heating-rate distribution calculated from equation (D1) with experimental results obtained from reference 17 for a Pioneer-type heat source (hexagonal cross section) tested at Mach number 6. The theoretical and experimental heating-rate distributions around the center cross section of the heat source are shown in figure 17 for a side-on, flat-face-forward orientation ($\sigma = 90°$, $\psi = 30°$). The trend of the data between the corners or edges of the flat face (between sonic points) is predicted well by the theory. The values near the stagnation point ($4s/w = 0$) are about 4 percent lower, and at the corner ($4s/w = 1$) about 8 percent higher than experiment. Around the corner ($1 \leqslant 4s/w \leqslant 3$) the agreement is poor. The schlieren photographs of reference 17 indicate the flow separates around the corner (note the sharp decrease in $\dot{q}/\dot{q}_{s,ref}$) and then reattaches, forming a secondary shock wave (note the gradual rise in $\dot{q}/\dot{q}_{s,ref}$ in the neighborhood of $1.4 \leqslant 4s/w \leqslant 2.0$). Since the present calculations assume the flow remains attached around the cross section to $4s/w = 3$, the poor agreement for $1 \leqslant 4s/w \leqslant 3$ is to be expected.

For roll orientations for which the shock wave is attached to a corner of the Isoloaf, $30.2° < |\psi| < 59.8°$, dimensionless heating-rate distributions were calculated from

$$\frac{\dot{q}[\psi,(2s/w)]}{\dot{q}_{s,ref}} = 0.463\left[\frac{R_{ref}}{(w/2)}\right]^{1/2}\left[\frac{1}{(\rho_1/\rho_s)C_{p_s}}\right]^{1/4}\left\{\frac{p[\psi,(2s/w)]}{p_s(\psi)}\,\frac{V_e[\psi,(2s/w)]}{V}\right\}^{1/2}\left[\frac{1}{|(2s/w) \pm 1|}\right]^{1/2} \tag{D5}$$

This result was obtained from equations (8) and (10) in reference 11; equation (10) was divided by equation (8) and the Newtonian expression was used for the stagnation-point velocity gradient.

When this result for the heating-rate distribution over a cone (referred to a unit sphere) is multiplied by $1/\sqrt{3}$ to convert to a wedge, equation (D5) is obtained. The quantities C_{p_s} and p/p_s were obtained from calculations noted in appendix A; ρ_1/ρ_s and V_e/V were evaluated from expressions in reference 12 for normal and oblique shock waves, respectively. A Newtonian variation in velocity was used around the curve surface of the Isoloaf.

For values of $\psi > 0°$ for which the bow shock wave is attached to a corner, the stagnation point is at $2s/w = -1$ and the plus sign is used in equation (D5); for $\psi < 0°$, it is at $2s/w = 1$ and the minus sign is used. At either corner, equation (D5) becomes infinite. This unrealistic situation is avoided by estimating the stagnation-point heating rate and fairing between the estimated value and lower values given by equation (D5). The maximum extent of faired values was for $-1.03 \leqslant 2s/w \leqslant -0.97$. The stagnation-point heating rate was estimated as follows: The heating rate calculated at the corner $2s/w = -1$ was plotted as a function of ψ for values of $\psi > 0°$ for which the bow shock is detached. (As the value of ψ for shock attachment is approached from either direction, the stagnation point approaches the corner.) These rates were faired for all $0° \leqslant \psi \leqslant 180°$. The estimated stagnation-point heating rates were obtained from the faired data at values of ψ for an attached shock wave.

APPENDIX E

ENTRY HEAT INPUT

Time histories of entry heating input to the thermal model were determined by coupling the heating-rate distributions with time histories of the Isoloaf rolling motion and reference heating rate. To simplify the coupling procedure, the dimensionless heating-rate distributions (appendix D) were averaged over each of the exterior nodes to obtain the nodal heating factors

$$F_i(\psi) = \frac{\int_i \frac{\dot{q}[\psi,(2s/w)]}{\dot{q}_{s,ref}} d\left(\frac{2s}{w}\right)}{\int_i d\left(\frac{2s}{w}\right)} \tag{E1}$$

as a function of ψ. Values of $F_i(\psi)$ are tabulated in table 8 for $-180° \leqslant \psi \leqslant 180°$ and $113 \leqslant i \leqslant 124$.

When the rate of change of heat-source motion was small compared to the rate of change of the reference heating rate, time histories of the heating rate applied to each node during entry were obtained from

$$\dot{q}_i(t) = F_i(\psi)\, \dot{q}_{s,ref}(t) \tag{E2}$$

where the value of ψ is that about which the oscillation occurred. Equation (E2), with $\psi = 0°$, was used during the side-on stable entries (cases 3 and 7).

For most of the other entries, the rate of change of heat-source motion was often significantly higher than the rate of change of the reference heating rate. For these periods, the heating factors were time-averaged to simulate the variation in each nodal heating factor with heat-source motion. During periods when the Isoloaf was spinning, the heating factors were averaged over a complete revolution; when it was oscillating, the time variation of the maximum amplitude of oscillation, $\Theta_A(t) = 0.5[\psi_{max,env}(t) - \psi_{min,env}(t)]$, was approximated by a step function $\Theta_{A_k}(\Delta t_k)$, as shown in figure 5. The heating factors were averaged over each time interval and weighted according to the relative length of time the Isoloaf spent at each orientation. For this purpose, it was assumed that the motion during each *kth* time interval Δt_k could be described as a function of time:

$$\Theta = \Theta_{A_k}(\Delta t_k) \cos\left(\frac{2\pi t}{t_p}\right) \tag{E3}$$

where Θ is the angular displacement measured from the value of ψ about which oscillation occurred and t_p is the period of oscillation. The amplitude of oscillation for each *kth* time interval was divided into j increments and the time-averaged heating factor for node i was calculated as follows:

$$\overline{F}_{ik}(\Delta t_k) = \frac{\sum_j F_i(\Theta_j) \left| \cos^{-1}(\Theta_{j+1}/\Theta_{A_k}) - \cos^{-1}(\Theta_j/\Theta_{A_k}) \right|}{2\pi} \tag{E4}$$

Finally, time histories of the heating rate applied to each node during entry were obtained from

$$\dot{q}_i(t) = \overline{F}_{ik}(\Delta t_k)\, \dot{q}_{s,ref}(t) \tag{E5}$$

for each successive Δt_k. The reference heating rate for each entry was obtained, of course, from the trajectory calculations.

REFERENCES

1. Burns, Raymond K.: Preliminary Analysis to Determine the Reentry Insulation Requirements on a Pioneer-Type Heat Source for Use in the Isotope Brayton Application. NASA TM X-52850, 1970.

2. Burns, Raymond K.: Preliminary Thermal Analysis of an Aerodynamically Shaped Heat Source for Use With the Isotope Brayton Power System. NASA TM X-52891, 1970.

3. Kaattari, George E.: Predicted Shock Envelopes About Two Types of Vehicles at Large Angles of Attack. NASA TN D-860, 1961.

4. Kaattari, George E.: Shock Envelopes of Blunt Bodies at Large Angles of Attack. NASA TN D-1980, 1963.

5. Kaattari, George E.: A Method for Predicting Shock Shapes and Pressure Distributions for a Wide Variety of Blunt Bodies at Zero Angle of Attack. NASA TN D-4539, 1968.

6. Tobak, M.; and Schiff, L. B.: A Nonlinear Aerodynamic Moment Formulation and Its Implications for Dynamic Stability Testing. AIAA Paper 71-275.

7. Gentry, A. E.: Hypersonic Arbitrary-Body Aerodynamic Computer Program (Mark III Version). Douglas Rep. DAC 61552, vol. 1, April 1968.

8. Peterson, Victor L.: Motions of a Short 10° Blunted Cone Entering a Martian Atmosphere at Arbitrary Angles of Attack and Arbitrary Pitching Rates. NASA TN D-1326, 1962.

9. Lewis, D. R.; Gaski, J. D.; and Thompson, L. R.: Chrysler Improved Numerical Differencing Analyzer for Third Generation Computers. NASA CR-99595, 1967.

10. Pappas, C. C.: The Calculation of Laminar Heat Transfer to the Windward Surfaces of a Straight-Wing Orbiter at High Angle of Attack and With Yaw. NASA TN D-6614, 1972.

11. Marvin, J. G.; and Pope, R. B.: Laminar Convective Heating and Ablation in the Mars Atmosphere. AIAA J., vol. 5, no. 2, Feb. 1967, pp. 240-248.

12. Ames Research Staff: Equations, Tables, and Charts for Compressible Flow. NACA Rep. 1135, 1953.

13. Hochstim, A. R.: Gas Properties Behind Shocks at Hypersonic Velocities. I. Normal Shocks in Air. Convair Rep. No. ZPh(GP)-002, Jan. 1957.

14. Inouye, M.; Marvin, J. G.; and Sinclair, A. R.: Comparison of Experimental and Theoretical Shock Shapes and Pressure Distributions on Flat-Faced Cylinders at Mach 10.5. NASA TN D-4397, 1968.

15. Dorrance, W. H.: Viscous Hypersonic Flow. McGraw-Hill, 1962, pp. 79–85.

16. Reshotko, E.: Heat Transfer to a General Three-Dimensional Stagnation Point. Jet Propulsion, vol. 47, Jan. 1958, pp. 58–60.

17. Hunt, J. L.: Heat Transfer to Four Fineness-Ratio – 1.6 Hexagonal Prisms at a Mach Number of 6. NASA TM X-2446, 1972.

TABLE 1 – HEAT SOURCE PHYSICAL AND THERMAL PROPERTIES

Component	Physical		Thermal		Thermo-physical
	Material	Thickness, mm	Conductivity, W/m °K	Emissivity	(specific heat) × density, J/m^3 °K
Fuel[a]	Plutonium dioxide	54.46 (dia)	9.70	b	3.83
Fuel liner	Tantalum, 10-percent tungsten	0.508	65.5	b	3.48
Strength member	Tantalum (T-111)	2.286	67.4	b	2.90
Clad[c]	Platinum, 20-percent rhodium	0.4572	70.8	0.85[c]	3.60
Insulation	Pyrolytic graphite	3 layers, 1.778 each	1.33 radially 209 circumferentially	0.5	4.64
Heat shield	POCO graphite	Variable	36.2 at 1366° K 29.4 at 1922° K 26.8 at 2478° K	0.8 0.8 0.8	3.48 at 1366° K 3.94 at 1922° K 4.18 at 2478° K

[a]Total thermal load = 400 W.

[b]Heat exchange by radiation across helium gaps neglected.

[c]Clad melting temperature = 2145° K; high emissivity coating assumed.

TABLE 2 – ENTRIES FOR THERMAL ANALYSIS

Case	Abort situation	Isoloaf initial conditions						Trajectory initial conditions at 121.92 km	
		Physical description	Attitude		Angular velocity				
			$\sigma_{i'}$, deg	$\psi_{i'}$, deg	$p_{B_{i'}}$, deg/sec	$q_{B_{i'}}$, deg/sec	$r_{B_{i'}}$, deg/sec	$V_{I_{i'}}$, km/sec	$\Gamma_{I_{i'}}$, deg
1	Launch	Side-on spinning	90	0	400	0	0	7.62	-7.7
2	↓	End-on spinning	0	↓	↓	↓	↓	↓	↓
3	↓	Side-on stable	90	0.1	0	↓	↓	↓	↓
4	Orbital decay	End-on spinning	0	0	400	↓	↓	7.83	-0.02
5	↓	End-on tumbling	↓	110	0	400	↓	↓	↓
6	Superorbital	Side-on spinning	90	0	400	0	↓	10.97	-10
7	↓	Side-on stable	↓	0.1	0	↓	↓	↓	↓

TABLE 3 – ISOLOAF MOTIONS AT PEAK ENTRY HEATING

Case	Abort situation	Initial attitude and motion	Oscillatory motion at peak heating		$\dot{q}_{s,ref,max}$ $\frac{MW}{m^2}$
			σ, deg	ψ, deg	
1	Launch	Side-on spinning	90 ±2	0 ±83	2.84
2	↓	End-on spinning	Large-angle coning and spinning motion		3.44
3	↓	Side-on stable	90 ±0.1	0 ±0.1	2.77
4	Orbital decay	End-on spinning	90 ±83	0 ±118	1.61
5	↓	End-on tumbling	90 ±31	0 ±57	1.41
6	Superorbital	Side-on spinning	90 ±0.5	0 ±55	8.97
7	↓	Side-on stable	90 ±0.1	0 ±0.1	8.65

TABLE 4 – PEAK TEMPERATURES (°K) OF CAPSULE CLAD AND ADJACENT SURFACES DURING ENTRY; GAPS OUTSIDE CLAD AIR FILLED

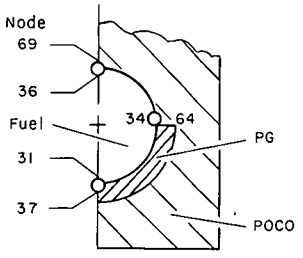

Case	Abort situation	Initial attitude and motion	Surface and node temperatures, °K					
			Clad, 31	PG, 37	Clad, 34	POCO, 64	Clad, 36	POCO, 69
1	Launch	Side-on spinning	1106*	1239*	1211	1494	1156	1233
2	↓	End-on spinning	1100*	1200*	1361	1656	1422	1633
3	↓	Side-on stable	1111*	1256*	1017*	1083*	933*	850*
4	Orbital decay	End-on spinning	1600*	1690*	1728	1900	1719	1806
5	↓	End-on tumbling	1706	1789	1617	1717	1544	1528
6	Superorbital	Side-on spinning	1183*	1422*	1456	1928	1294	1422*
7	↓	Side-on stable	1158*	1395*	1061*	1244*	947*	872*

*Not peak temperature; value reached at termination of entry.

TABLE 5 – ISOLOAF AERODYNAMIC COEFFICIENTS

ψ, deg \ σ, deg	0	5	10	20	25	35	50	65	70	80	85	90
						$C_{A_o}(\sigma,\psi)$						
0[a]	0.9780	0.9730	0.9680	0.9310	0.9000	0.7920	0.4900	0.2100	0.1370	0.0339	0.0100	0.0
10	1.0000	0.9920	0.9690	0.8830	0.8210	0.6710	0.4130	0.1780	0.1170	0.0301	0.0076	0.0
90	1.0000	0.9920	0.9690	0.8830	0.8210	0.6710	0.4130	0.1780	0.1170	0.0301	0.0076	0.0
180	1.0000	0.9920	0.9690	0.8830	0.8210	0.6710	0.4130	0.1780	0.1170	0.0301	0.0076	0.0
						$C_{N_o}(\sigma,\psi)$						
0	0.0	0.0211	0.0620	0.2510	0.3860	0.7170	1.2800	1.6420	1.7020	1.7700	1.7820	1.7870
10	0.0	0.0135	0.0537	0.2080	0.3180	0.5860	1.0440	1.4620	1.5720	1.7260	1.7670	1.7530
20	0.0	0.0122	0.0486	0.1880	0.2880	0.5300	0.9450	1.3230	1.4220	1.5620	1.5980	1.6830
25	0.0	0.0115	0.0458	0.1780	0.2710	0.4990	0.8900	1.2460	1.3400	1.4720	1.5060	1.6600
35	0.0	0.0104	0.0412	0.1600	0.2440	0.4490	0.8010	1.1210	1.2060	1.3240	1.3540	1.5930
45	0.0	0.0099	0.0395	0.1530	0.2340	0.4310	0.7700	1.0770	1.1580	1.2720	1.3020	1.5390
55	0.0	0.0105	0.0417	0.1620	0.2470	0.4550	0.8120	1.1360	1.2210	1.3410	1.3720	1.5950
65	0.0	0.0118	0.0470	0.1820	0.2790	0.5130	0.9160	1.2820	1.3780	1.5140	1.5490	1.6950
70	0.0	0.0127	0.0504	0.1960	0.2990	0.5500	0.9810	1.3730	1.4760	1.6210	1.6590	1.7450
80	0.0	*0.0144*	*0.0570*	*0.2210*	*0.3370*	*0.6210*	*1.1080*	*1.5510*	*1.6670*	*1.8310*	*1.8740*	*1.8500*
90	0.0	0.0154	0.0610	0.2360	0.3610	0.6650	1.1860	1.6600	1.7850	1.9610	2.0060	1.9240
100	0.0	0.0153	0.0607	0.2350	0.3590	0.6620	1.1800	1.6520	1.7760	1.9510	1.9960	1.9300
110	0.0	0.0144	0.0568	0.2210	0.3370	0.6200	1.1070	1.5490	1.6650	1.8290	1.8720	1.8880
120	0.0	0.0130	0.0515	0.2000	0.3050	0.5620	1.0030	1.4040	1.5090	1.6570	1.6960	1.7950
140	0.0	0.0110	0.0436	0.1690	0.2580	0.4760	0.8490	1.1880	1.2780	1.4030	1.4360	1.6080
155	0.0	0.0110	0.0438	0.1700	0.2590	0.4780	0.8520	1.1940	1.2830	1.4090	1.4420	1.5000
160	0.0	0.0113	0.0448	0.1740	0.2660	0.4890	0.8730	1.2210	1.3130	1.4420	1.4760	1.4960
170	0.0	0.0119	0.0472	0.1830	0.2800	0.5150	0.9190	1.2860	1.3830	1.5190	1.5540	1.5380
180	0.0	0.0122	0.0484	0.1880	0.2870	0.5290	0.9430	1.3200	1.4190	1.5580	1.5940	1.5530
						$C_{Y_o}(\sigma,\psi)$						
0	0.0	0.0	0.0	0.0	0.0	0.0	0.0	0.0	0.0	0.0	0.0	0.0
10	0.0	0.0020	0.0078	0.0303	0.0462	0.0852	0.1520	0.2130	0.2290	0.2510	0.2570	0.2480
20	0.0	0.0027	0.0109	0.0421	0.0643	0.1180	0.2110	0.2960	0.3180	0.3490	0.3570	0.3510
25	0.0	0.0026	0.0104	0.0406	0.0620	0.1140	0.2040	0.2850	0.3060	0.3370	0.3440	0.3470
35	0.0	0.0016	0.0064	0.0248	0.0378	0.0698	0.1240	0.1740	0.1870	0.2060	0.2100	0.2450
45	0.0	-0.0001	-0.0004	-0.0019	-0.0027	-0.0052	-0.0092	-0.0129	-0.0137	-0.0152	-0.0153	-0.0195
55	0.0	-0.0019	-0.0076	-0.0294	-0.0449	-0.0826	-0.1470	-0.2060	-0.2220	-0.2440	-0.2490	-0.3000
65	0.0	-0.0031	-0.0123	-0.0478	-0.0728	-0.1340	-0.2390	-0.3350	-0.3600	-0.3950	-0.4050	-0.3920
70	0.0	*-0.0033*	*-0.0131*	*-0.0508*	-0.0777	*-0.1430*	*-0.2550*	*-0.3570*	*-0.3840*	*-0.4220*	*-0.4310*	*-0.3960*
80	0.0	-0.0023	-0.0109	-0.0423	-0.0646	-0.1190	-0.2120	-0.2970	-0.3200	-0.3510	-0.3590	-0.2950
90	0.0	-0.0009	-0.0037	-0.0145	-0.0221	-0.0407	-0.0726	-0.1020	-0.1090	-0.1200	-0.1230	-0.0955
100	0.0	0.0011	0.0045	0.0172	0.0264	0.0486	0.0867	0.1210	0.1300	0.1430	0.1460	0.1140
110	0.0	0.0025	0.0094	0.0366	0.0556	0.1020	0.1820	0.2550	0.2750	0.3020	0.3090	0.2780
120	0.0	0.0026	0.0104	0.0403	0.0615	0.1130	0.2020	0.2830	0.3040	0.3340	0.3420	0.3000
140	0.0	0.0008	0.0033	0.0128	0.0194	0.0358	0.0642	0.0898	0.0965	0.1060	0.1080	0.0830
155	0.0	-0.0008	-0.0033	-0.0127	-0.0193	-0.0355	-0.0634	-0.0888	-0.0955	-0.1050	-0.1070	-0.0775
160	0.0	-0.0011	-0.0044	-0.0170	-0.0260	-0.0480	-0.0855	-0.1200	-0.1290	-0.1410	-0.1450	-0.1120
170	0.0	-0.0010	-0.0041	-0.0158	-0.0241	-0.0444	-0.0794	-0.1110	-0.1190	-0.1310	-0.1340	-0.1300
180	0.0	0.0	0.0	0.0	0.0	0.0	0.0	0.0	0.0	0.0	0.0	0.0
						$C_{l_o}(\sigma,\psi)$						
0	0.0	0.0	0.0	0.0	0.0	0.0	0.0	0.0	0.0	0.0	0.0	0.0
10	0.0	0.0	0.0	-0.0000	-0.0000	-0.0000	-0.0001	-0.0001	-0.0001	-0.0001	-0.0001	-0.0081
20	0.0	-0.0000	-0.0000	-0.0001	-0.0002	-0.0003	-0.0006	-0.0009	-0.0009	-0.0010	-0.0011	-0.0202
25	0.0	-0.0000	-0.0001	-0.0002	-0.0004	-0.0007	-0.0012	-0.0017	-0.0018	-0.0020	-0.0020	-0.0220
35	0.0	-0.0000	-0.0002	-0.0006	-0.0009	-0.0017	-0.0030	-0.0043	-0.0046	-0.0050	-0.0052	-0.0080
45	0.0	-0.0001	-0.0003	-0.0012	-0.0018	-0.0033	-0.0059	-0.0082	-0.0089	-0.0097	-0.0100	-0.0120
55	0.0	-0.0001	-0.0005	-0.0019	-0.0029	-0.0054	-0.0096	-0.0134	-0.0144	-0.0158	-0.0162	-0.0178
65	0.0	-0.0002	-0.0007	-0.0027	-0.0042	-0.0077	-0.0137	-0.0192	-0.0206	-0.0227	-0.0232	-0.0020
70	0.0	-0.0002	-0.0008	-0.0031	-0.0048	-0.0089	-0.0158	-0.0222	-0.0238	-0.0262	-0.0268	-0.0055
80	0.0	-0.0002	-0.0010	-0.0039	-0.0060	-0.0110	-0.0197	-0.0275	-0.0296	-0.0325	-0.0333	-0.0225
90	0.0	-0.0003	-0.0012	-0.0045	-0.0069	-0.0126	-0.0225	-0.0315	-0.0339	-0.0372	-0.0381	-0.0358
100	0.0	-0.0003	-0.0012	-0.0048	-0.0073	-0.0134	-0.0239	-0.0334	-0.0359	-0.0394	-0.0404	-0.0411
110	0.0	-0.0003	-0.0012	-0.0047	-0.0072	-0.0133	-0.0237	-0.0332	-0.0357	-0.0392	-0.0401	-0.0423
120	0.0	-0.0003	-0.0011	-0.0044	-0.0068	-0.0125	-0.0222	-0.0311	-0.0335	-0.0368	-0.0376	-0.0416
140	0.0	-0.0002	-0.0008	-0.0033	-0.0050	-0.0092	-0.0164	-0.0230	-0.0247	-0.0272	-0.0278	-0.0300
155	0.0	-0.0001	-0.0005	-0.0021	-0.0032	-0.0059	-0.0106	-0.0148	-0.0159	-0.0175	-0.0179	-0.0053
160	0.0	-0.0001	-0.0004	-0.0017	-0.0026	-0.0048	-0.0085	-0.0119	-0.0128	-0.0141	-0.0144	-0.0040
170	0.0	-0.0001	-0.0002	-0.0008	-0.0013	-0.0024	-0.0043	-0.0060	-0.0064	-0.0071	-0.0072	-0.0039
180	0.0	0.0	0.0	0.0	0.0	0.0	0.0	0.0	0.0	0.0	0.0	0.0
						$C_{m_o}(\sigma,\psi)$						
0	0.0463	0.0450	0.0408	0.0321	0.0282	0.0385	0.0240	0.0480	0.0465	0.0185	0.0076	0.0
10	0.0428	0.0425	0.0416	0.0378	0.0352	0.0287	0.0177	0.0076	0.0050	0.0013	0.0003	0.0
20	0.0408	0.0405	0.0396	0.0360	0.0335	0.0274	0.0169	0.0073	0.0048	0.0012	0.0003	0.0
25	0.0394	0.0391	0.0382	0.0348	0.0324	0.0264	0.0163	0.0070	0.0046	0.0012	0.0003	0.0
35	0.0356	0.0353	0.0345	0.0314	0.0292	0.0239	0.0147	0.0064	0.0042	0.0011	0.0003	0.0
45	0.0307	0.0305	0.0298	0.0271	0.0252	0.0206	0.0127	0.0055	0.0036	0.0009	0.0002	0.0
55	0.0249	0.0247	0.0242	0.0220	0.0205	0.0167	0.0103	0.0044	0.0029	0.0007	0.0002	0.0
65	0.0184	0.0182	0.0178	0.0162	0.0151	0.0123	0.0076	0.0033	0.0021	0.0005	0.0001	0.0
70	0.0149	0.0148	0.0144	0.0131	0.0122	0.0100	0.0061	0.0026	0.0017	0.0004	0.0001	0.0

[a]Non-newtonian theory, references 3-5.

TABLE 5 – ISOLOAF AERODYNAMIC COEFFICIENTS – Concluded

ψ, deg \ σ, deg	0	5	10	20	25	35	50	65	70	80	85	90
$C_{m_o}(\sigma,\psi)$ (Continued)												
80	0.0075	0.0075	0.0073	0.0067	0.0062	0.0051	0.0031	0.0013	0.0009	0.0002	0.0001	0.0
90	0.0	0.0	0.0	0.0	0.0	0.0	0.0	0.0	0.0	0.0	0.0	0.0
100	-0.0075	-0.0075	-0.0073	-0.0067	-0.0062	-0.0051	-0.0031	-0.0013	-0.0009	-0.0002	-0.0001	0.0
110	-0.0149	-0.0148	-0.0144	-0.0131	-0.0122	-0.0100	-0.0061	-0.0026	-0.0017	-0.0004	-0.0001	0.0
120	-0.0217	-0.0216	-0.0211	-0.0192	-0.0178	-0.0146	-0.0090	-0.0039	-0.0025	-0.0006	-0.0002	0.0
140	-0.0333	-0.0330	-0.0323	-0.0294	-0.0273	-0.0223	-0.0138	-0.0059	-0.0039	-0.0010	-0.0002	0.0
155	-0.0394	-0.0391	-0.0382	-0.0348	-0.0324	-0.0264	-0.0163	-0.0070	-0.0046	-0.0012	-0.0003	0.0
160	-0.0408	-0.0405	-0.0396	-0.0360	-0.0335	-0.0274	-0.0169	-0.0073	-0.0048	-0.0012	-0.0003	0.0
170	-0.0428	-0.0425	-0.0415	-0.0378	-0.0352	-0.0287	-0.0177	-0.0076	-0.0050	-0.0013	-0.0003	0.0
180	-0.0463	-0.0450	-0.0408	-0.0321	-0.0282	-0.0385	-0.0240	-0.0480	-0.0465	-0.0185	-0.0076	0.0
$C_{m_{\dot\sigma}}(\sigma,\psi)$												
0	-0.0402	-0.0401	-0.0396	-0.0378	-0.0365	-0.0330	-0.0259	-0.0170	-0.0138	-0.0070	-0.0035	0.0
20	-0.0392	-0.0390	-0.0386	-0.0368	-0.0355	-0.0321	-0.0252	-0.0166	-0.0134	-0.0068	-0.0034	0.0
40	-0.0365	-0.0364	-0.0360	-0.0343	-0.0331	-0.0299	-0.0235	-0.0154	-0.0125	-0.0063	-0.0032	0.0
60	-0.0335	-0.0333	-0.0329	-0.0315	-0.0303	-0.0274	-0.0215	-0.0142	-0.0115	-0.0058	-0.0029	0.0
80	-0.0315	-0.0314	-0.0310	-0.0296	-0.0285	-0.0258	-0.0203	-0.0133	-0.0108	-0.0054	-0.0027	0.0
100	-0.0315	-0.0314	-0.0310	-0.0296	-0.0285	-0.0258	-0.0203	-0.0133	-0.0108	-0.0054	-0.0027	0.0
120	-0.0335	-0.0333	-0.0329	-0.0315	-0.0303	-0.0274	-0.0215	-0.0142	-0.0115	-0.0058	-0.0029	0.0
140	-0.0365	-0.0364	-0.0360	-0.0343	-0.0331	-0.0299	-0.0235	-0.0154	-0.0125	-0.0063	-0.0032	0.0
160	-0.0392	-0.0390	-0.0386	-0.0368	-0.0355	-0.0321	-0.0252	-0.0166	-0.0134	-0.0068	-0.0034	0.0
180	-0.0402	-0.0401	-0.0396	-0.0378	-0.0365	-0.0330	-0.0259	-0.0170	-0.0138	-0.0070	-0.0035	0.0
$C_{m_{\dot\phi}}(\sigma,\psi)/\delta$												
0	0.0	0.0	0.0	0.0	0.0	0.0	0.0	0.0	0.0	0.0	0.0	0.0
20	-0.0029	-0.0029	-0.0029	-0.0027	-0.0026	-0.0024	-0.0019	-0.0012	-0.0010	-0.0005	-0.0003	0.0
40	-0.0044	-0.0044	-0.0044	-0.0042	-0.0040	-0.0036	-0.0029	-0.0019	-0.0015	-0.0008	-0.0004	0.0
60	-0.0039	-0.0039	-0.0038	-0.0037	-0.0035	-0.0032	-0.0025	-0.0016	-0.0013	-0.0007	-0.0003	0.0
80	-0.0015	-0.0015	-0.0015	-0.0014	-0.0014	-0.0013	-0.0010	-0.0006	-0.0005	-0.0003	-0.0001	0.0
100	0.0015	0.0015	0.0015	0.0014	0.0014	0.0013	0.0010	0.0006	0.0005	0.0003	0.0001	0.0
120	0.0039	0.0039	0.0038	0.0037	0.0035	0.0032	0.0025	0.0016	0.0013	0.0007	0.0003	0.0
140	0.0044	0.0044	0.0044	0.0042	0.0040	0.0036	0.0029	0.0019	0.0015	0.0008	0.0004	0.0
160	0.0029	0.0029	0.0029	0.0027	0.0026	0.0024	0.0019	0.0012	0.0010	0.0005	0.0003	0.0
180	0.0	0.0	0.0	0.0	0.0	0.0	0.0	0.0	0.0	0.0	0.0	0.0
$C_{n_o}(\sigma,\psi)$												
0	0.0	0.0	0.0	0.0	0.0	0.0	0.0	0.0	0.0	0.0	0.0	0.0
10	0.0075	0.0075	0.0073	0.0067	0.0062	0.0051	0.0031	0.0013	0.0009	0.0002	0.0001	0.0
20	0.0149	0.0148	0.0144	0.0131	0.0122	0.0100	0.0061	0.0026	0.0017	0.0004	0.0001	0.0
25	0.0184	0.0182	0.0178	0.0162	0.0151	0.0123	0.0076	0.0033	0.0021	0.0005	0.0001	0.0
35	0.0249	0.0247	0.0242	0.0220	0.0205	0.0167	0.0103	0.0044	0.0029	0.0007	0.0002	0.0
45	0.0307	0.0305	0.0298	0.0271	0.0252	0.0206	0.0127	0.0055	0.0036	0.0009	0.0002	0.0
55	0.0356	0.0353	0.0345	0.0314	0.0292	0.0239	0.0147	0.0064	0.0042	0.0011	0.0003	0.0
65	0.0394	0.0391	0.0382	0.0348	0.0324	0.0264	0.0163	0.0070	0.0046	0.0012	0.0003	0.0
70	0.0408	0.0405	0.0396	0.0360	0.0335	0.0274	0.0169	0.0073	0.0048	0.0012	0.0003	0.0
80	0.0428	0.0425	0.0415	0.0378	0.0352	0.0287	0.0177	0.0076	0.0050	0.0013	0.0003	0.0
90	0.0435	0.0431	0.0422	0.0384	0.0357	0.0292	0.0180	0.0078	0.0051	0.0013	0.0003	0.0
100	0.0428	0.0425	0.0415	0.0378	0.0352	0.0287	0.0177	0.0076	0.0050	0.0013	0.0003	0.0
110	0.0408	0.0405	0.0396	0.0360	0.0335	0.0274	0.0169	0.0073	0.0048	0.0012	0.0003	0.0
120	0.0376	0.0374	0.0365	0.0332	0.0309	0.0252	0.0156	0.0067	0.0044	0.0011	0.0003	0.0
140	0.0279	0.0277	0.0271	0.0247	0.0229	0.0187	0.0115	0.0050	0.0033	0.0008	0.0002	0.0
155	0.0184	0.0182	0.0178	0.0162	0.0151	0.0123	0.0076	0.0033	0.0021	0.0005	0.0001	0.0
160	0.0149	0.0148	0.0144	0.0131	0.0122	0.0100	0.0061	0.0026	0.0017	0.0004	0.0001	0.0
170	0.0075	0.0075	0.0073	0.0067	0.0062	0.0051	0.0031	0.0013	0.0009	0.0002	0.0001	0.0
180	0.0	0.0	0.0	0.0	0.0	0.0	0.0	0.0	0.0	0.0	0.0	0.0
$C_{n_{\dot\sigma}}(\sigma,\psi)$												
0	0.0	0.0	0.0	0.0	0.0	0.0	0.0	0.0	0.0	0.0	0.0	0.0
20	-0.0029	-0.0029	-0.0029	-0.0027	-0.0026	-0.0024	-0.0019	-0.0012	-0.0010	-0.0005	-0.0003	0.0
40	-0.0044	-0.0044	-0.0044	-0.0042	-0.0040	-0.0036	-0.0029	-0.0019	-0.0015	-0.0008	-0.0004	0.0
60	-0.0039	-0.0039	-0.0038	-0.0037	-0.0035	-0.0032	-0.0025	-0.0016	-0.0013	-0.0007	-0.0003	0.0
80	-0.0015	-0.0015	-0.0015	-0.0014	-0.0014	-0.0013	-0.0010	-0.0006	-0.0005	-0.0003	-0.0001	0.0
100	0.0015	0.0015	0.0015	0.0014	0.0014	0.0013	0.0010	0.0006	0.0005	0.0003	0.0001	0.0
120	0.0039	0.0039	0.0038	0.0037	0.0035	0.0032	0.0025	0.0016	0.0013	0.0007	0.0003	0.0
140	0.0044	0.0044	0.0044	0.0042	0.0040	0.0036	0.0029	0.0019	0.0015	0.0008	0.0004	0.0
160	0.0029	0.0029	0.0029	0.0027	0.0026	0.0024	0.0019	0.0012	0.0010	0.0005	0.0003	0.0
180	0.0	0.0	0.0	0.0	0.0	0.0	0.0	0.0	0.0	0.0	0.0	0.0
$C_{n_{\dot\phi}}(\sigma,\psi)/\delta$												
0	-0.0312	-0.0311	-0.0307	-0.0294	-0.0283	-0.0256	-0.0201	-0.0132	-0.0107	-0.0054	-0.0027	0.0
20	-0.0323	-0.0322	-0.0318	-0.0303	-0.0292	-0.0265	-0.0208	-0.0136	-0.0110	-0.0056	-0.0028	0.0
40	-0.0350	-0.0348	-0.0344	-0.0329	-0.0317	-0.0286	-0.0225	-0.0148	-0.0120	-0.0061	-0.0030	0.0
60	-0.0380	-0.0378	-0.0374	-0.0357	-0.0344	-0.0312	-0.0244	-0.0160	-0.0130	-0.0066	-0.0033	0.0
80	-0.0400	-0.0398	-0.0394	-0.0376	-0.0362	-0.0328	-0.0257	-0.0169	-0.0136	-0.0070	-0.0035	0.0
100	-0.0400	-0.0398	-0.0394	-0.0376	-0.0362	-0.0328	-0.0257	-0.0169	-0.0136	-0.0070	-0.0035	0.0
120	-0.0380	-0.0378	-0.0374	-0.0357	-0.0344	-0.0312	-0.0244	-0.0160	-0.0130	-0.0066	-0.0033	0.0
140	-0.0350	-0.0348	-0.0344	-0.0329	-0.0317	-0.0286	-0.0225	-0.0148	-0.0120	-0.0061	-0.0030	0.0
160	-0.0323	-0.0322	-0.0318	-0.0303	-0.0292	-0.0265	-0.0208	-0.0136	-0.0110	-0.0056	-0.0028	0.0
180	-0.0312	-0.0311	-0.0307	-0.0294	-0.0283	-0.0256	-0.0201	-0.0132	-0.0107	-0.0054	-0.0027	0.0

TABLE 6 – AERODYNAMIC SYMMETRY RELATIONSHIPS

$90° < \sigma \leqslant 180°$	For negative ψ
$C_{A_o}(\sigma, \psi) = -C_{A_o}(180° - \sigma, \psi)$	$C_{Y_o}(\sigma, -\psi) = -C_{Y_o}(\sigma, \psi)$
$C_{m_o}(\sigma, \psi) = -C_{m_o}(180° - \sigma, \psi)$	$C_{l_o}(\sigma, -\psi) = -C_{l_o}(\sigma, \psi)$
$C_{n_o}(\sigma, \psi) = -C_{n_o}(180° - \sigma, \psi)$	$C_{m_{\dot{\phi}}}(\sigma, -\psi) = -C_{m_{\dot{\phi}}}(\sigma, \psi)$
For all other coefficients	$C_{n_o}(\sigma, -\psi) = -C_{n_o}(\sigma, \psi)$
$C_x(\sigma, \psi) = C_x(180° - \sigma, \psi)$	$C_{n_{\dot{\sigma}}}(\sigma, \psi) = -C_{n_{\dot{\sigma}}}(\sigma, \psi)$
	For all other coefficients
	$C_x(\sigma, -\psi) = C_x(\sigma, \psi)$

TABLE 7 – STAGNATION-POINT VELOCITY GRADIENTS FOR ISOLOAF ORIENTATIONS WITH DETACHED BOW WAVE, $\sigma = 90°$

ψ, deg	$\frac{d(V_e/V)}{d(2s/w)}$
0	0.0774
10	0.0940
20	0.1375
28	0.2490
62	0.2190
90	0.0720
135	0.8488
150	0.3300
160	0.1750
180	0.0900

TABLE 8 – HEATING FACTORS $F_i(\psi)$ FOR ISOLOAF EXTERIOR SURFACE NODES

Node i / ψ, deg	113	114	115	116	117	118	119	120	121	122	123	124
-180	0.0200	0.0200	0.0200	0.0200	0.0200	0.0200	0.0200	0.0200	0.0200	1.103	2.236	1.633
-160	0.0155	0.0155	0.0155	0.432	0.464	0.495	0.530	0.578	0.655	2.087	1.982	1.782
-150	0.0134	0.0134	0.0134	0.598	0.651	0.704	0.767	0.859	1.023	2.257	2.499	1.983
-135	0.0105	0.0105	0.0105	0.751	0.833	0.922	1.035	1.224	1.666	3.340	2.413	1.339
-90	0.0182	0.0182	0.0182	1.764	1.358	1.227	1.228	1.401	1.607	1.735	0.164	0.0182
-62	0.879	1.020	1.712	2.194	1.736	1.544	1.380	1.246	1.149	0.598	0.0108	0.0108
-58	1.114	1.358	2.729	2.963	1.554	1.246	1.080	0.961	0.853	0.595	0.0104	0.0104
-45	1.320	1.609	3.195	3.242	1.695	1.359	1.179	1.048	0.945	0.447	0.0098	0.0098
-32	1.210	1.475	2.927	2.776	1.431	1.147	0.995	0.884	0.806	0.293	0.0104	0.0104
-28	1.551	1.757	2.342	1.954	1.145	0.941	0.826	0.742	0.678	0.188	0.0116	0.0116
-20	1.542	1.592	2.085	1.255	0.819	0.701	0.629	0.573	0.529	0.127	0.0148	0.0148
-10	1.434	1.443	1.883	0.485	0.284	0.267	0.253	0.242	0.236	0.0340	0.0222	0.0222
0	1.363	1.423	1.844	0.0273	0.0273	0.0273	0.0273	0.0273	0.0273	0.0273	0.0273	0.0273
10	1.418	1.443	1.662	0.0222	0.0222	0.0222	0.0222	0.0222	0.0222	0.0222	0.0222	0.0222
20	1.500	1.458	1.426	0.0148	0.0148	0.0148	0.0148	0.0148	0.0148	0.0148	0.0148	0.0148
28	1.398	1.282	1.187	0.0116	0.0116	0.0116	0.0116	0.0116	0.0116	0.0116	0.0116	0.0116
32	1.062	0.952	0.847	0.0107	0.0107	0.0107	0.0107	0.0107	0.0107	0.0107	0.0107	0.0107
45	1.159	1.038	0.924	0.0098	0.0098	0.0098	0.0098	0.0098	0.0098	0.0098	0.0098	0.0098
58	0.978	0.877	0.780	0.0104	0.0104	0.0104	0.0104	0.0104	0.0104	0.0104	0.0104	0.0104
62	0.762	0.688	0.616	0.0108	0.0108	0.0108	0.0108	0.0108	0.0108	0.0108	0.0108	0.0108
90	0.0182	0.0182	0.0182	0.0182	0.0182	0.0182	0.0182	0.0182	0.0182	0.0182	0.0182	0.0182
135	0.0105	0.0105	0.0105	0.0105	0.0105	0.0105	0.0105	0.0105	0.0105	0.0588	0.883	1.064
150	0.0134	0.0134	0.0134	0.0134	0.0134	0.0134	0.0134	0.0134	0.0134	0.172	1.300	1.609
160	0.0155	0.0155	0.0155	0.0155	0.0155	0.0155	0.0155	0.0155	0.0155	0.352	1.629	1.707
180	0.0200	0.0200	0.0200	0.0200	0.0200	0.0200	0.0200	0.0200	0.0200	1.103	2.236	1.633

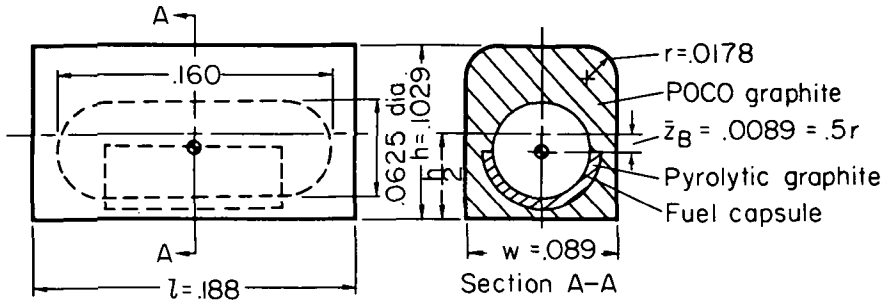

Note: all dimensions in meters

Mass, kg	Moment of inertia, kg-m^2		
	I_{x_B}	I_{y_B}	I_{z_B}
5.77	.00641	.0171	.0161

(a) Overall dimensions and mass properties.

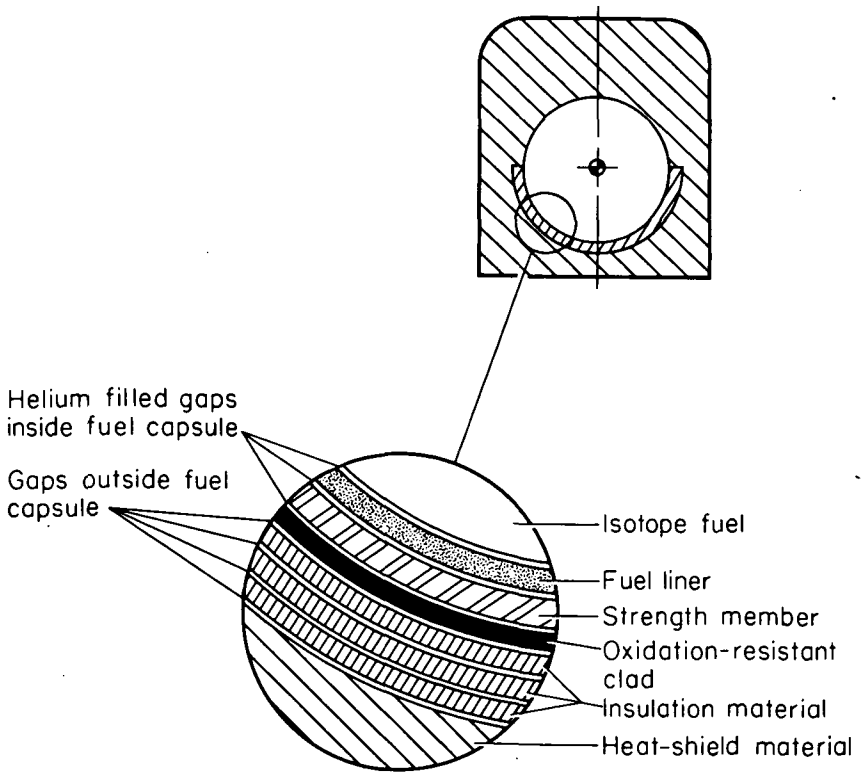

(b) Layered arrangement of internal components.

Figure 1.– Isoloaf heat source.

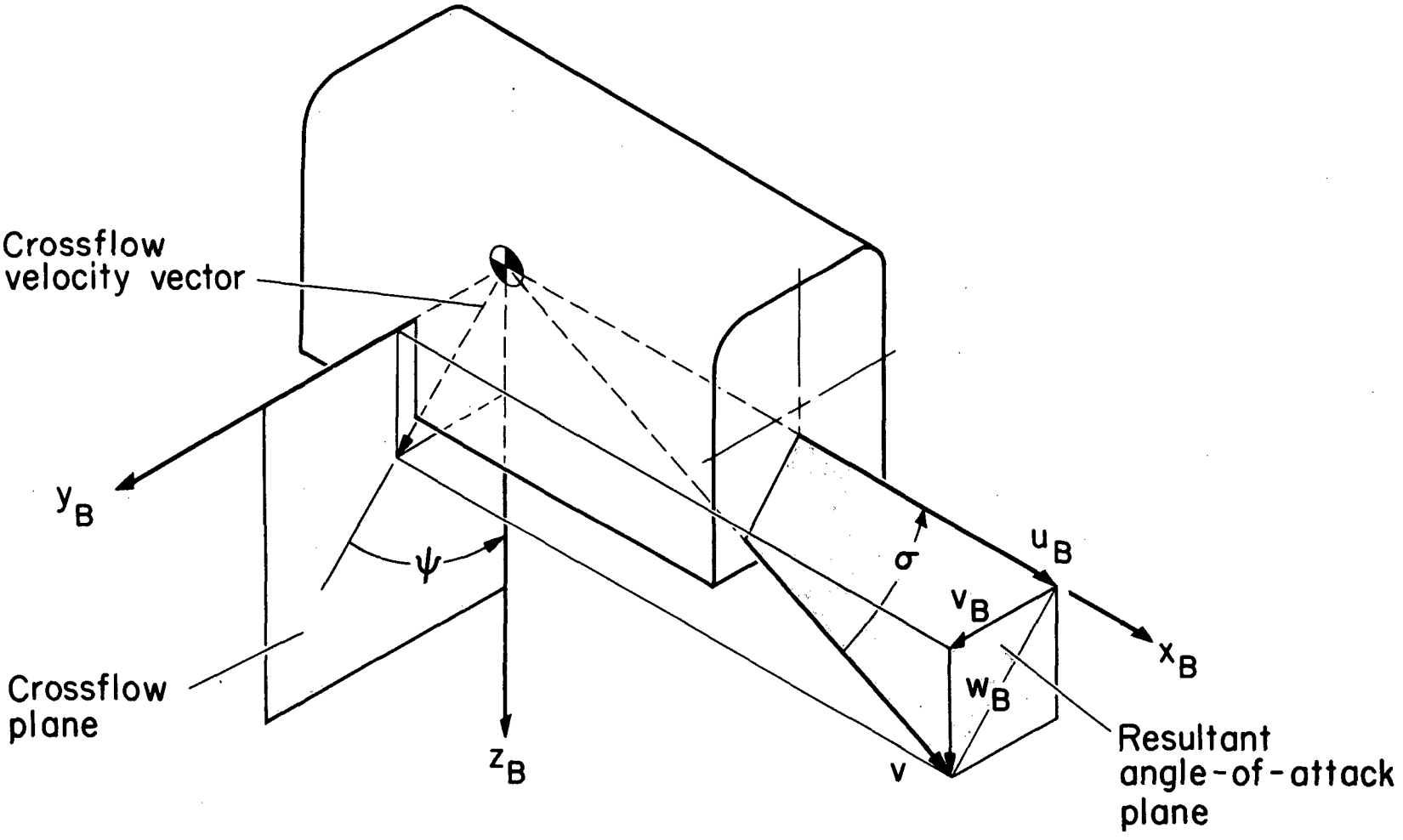

Figure 2.– Axes, angles, and velocity components for Isoloaf orientation in flight.

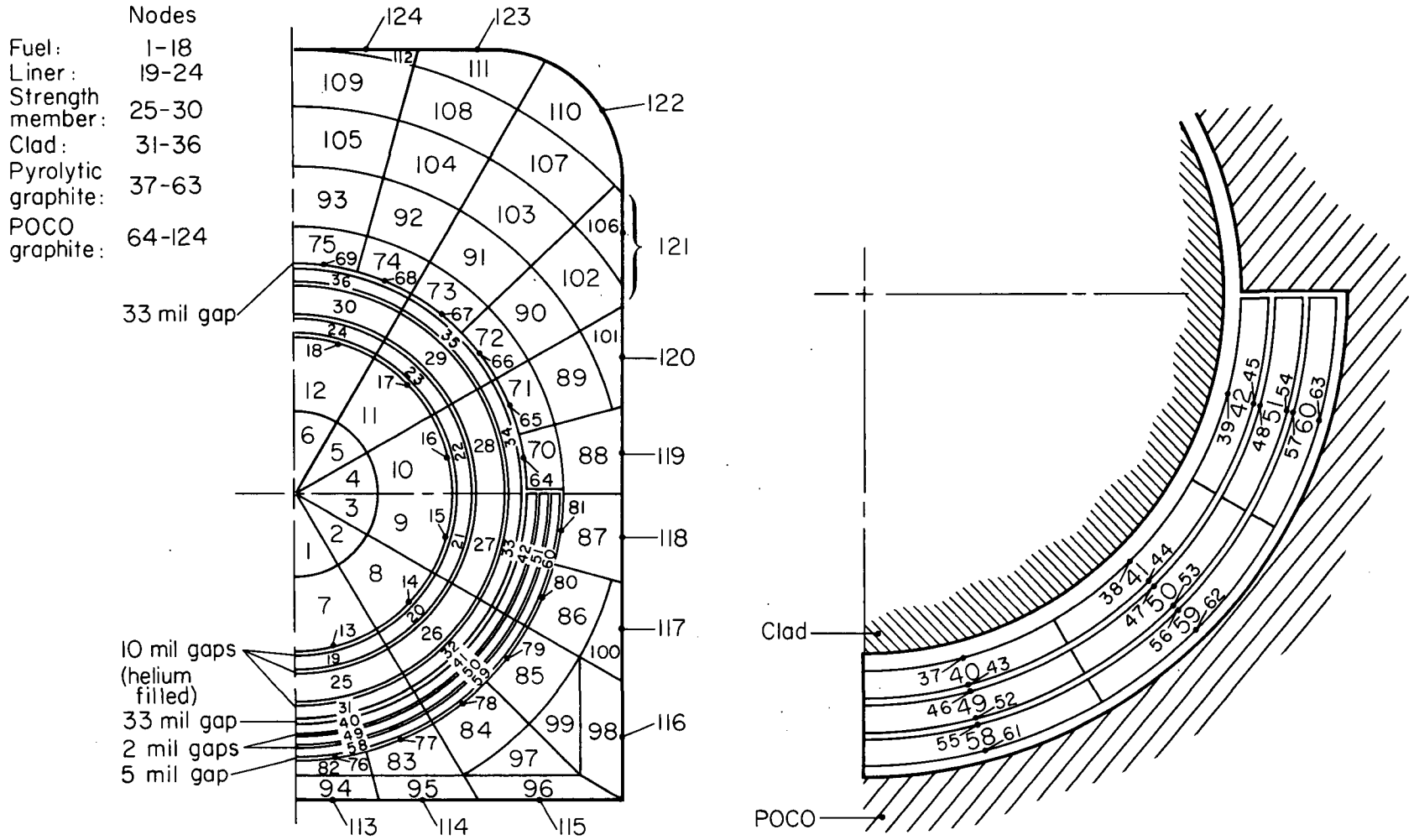

(a) Complete model.

(b) Pyrolytic graphite insulation nodes.

Figure 3.– Isoloaf two-dimensional thermal model.

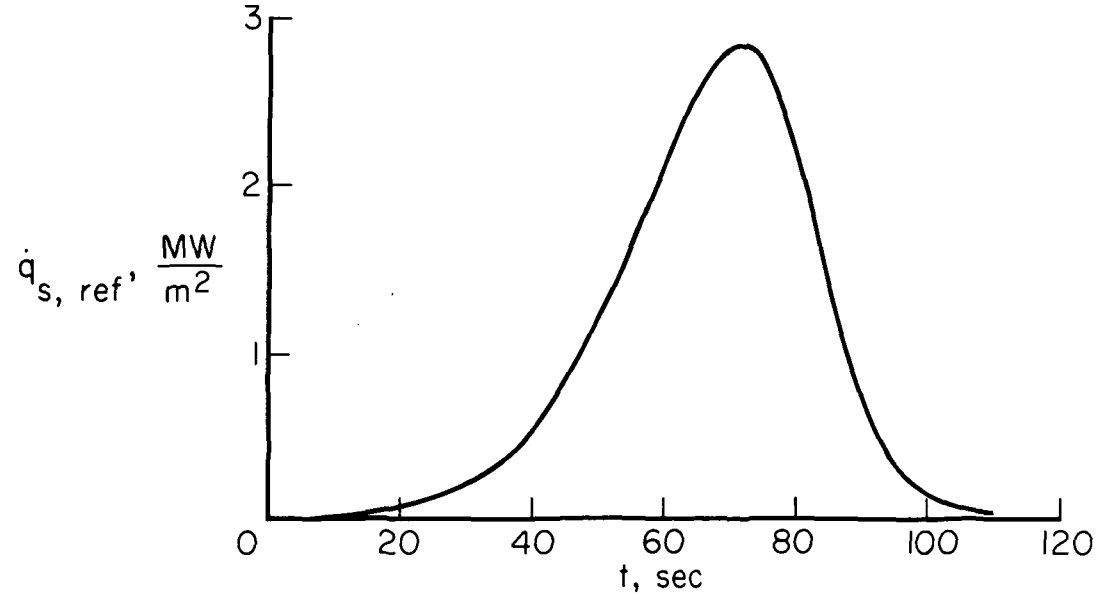

Figure 4.– Reference heating-rate time history during launch-abort entry with Isoloaf initially spinning side-on; case 1.

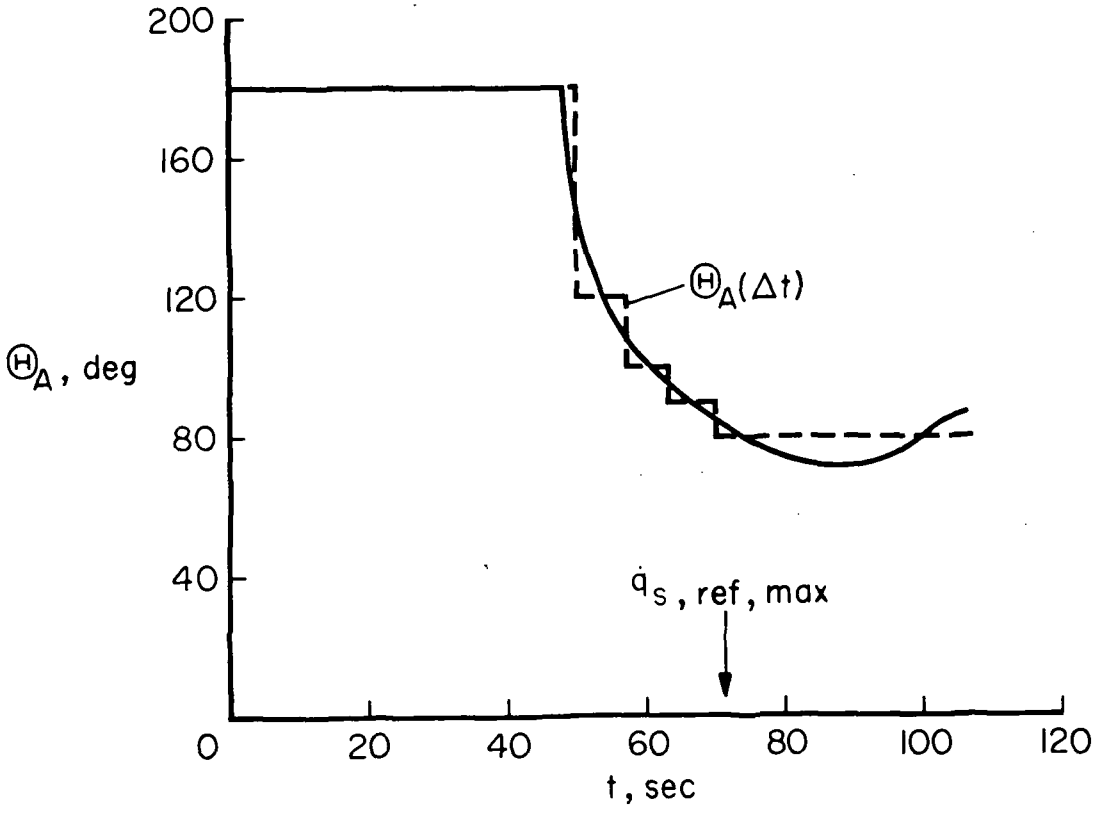

Figure 5.– Rolling-motion time history during launch-abort entry with Isoloaf initially spinning side-on; case 1.

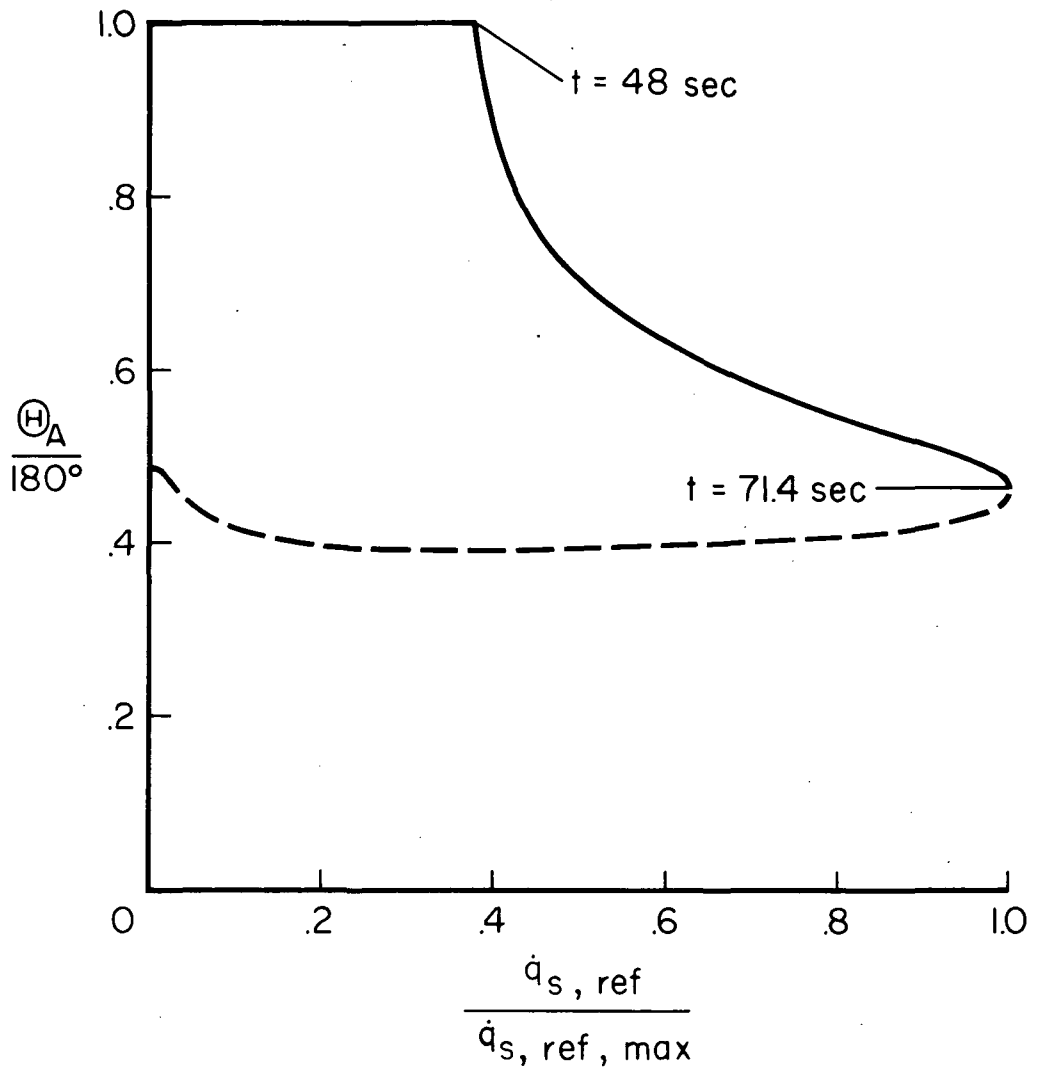

Figure 6.– Rolling motion relative to reference heating rate during launch-abort entry with Isoloaf initially spinning side-on; case 1.

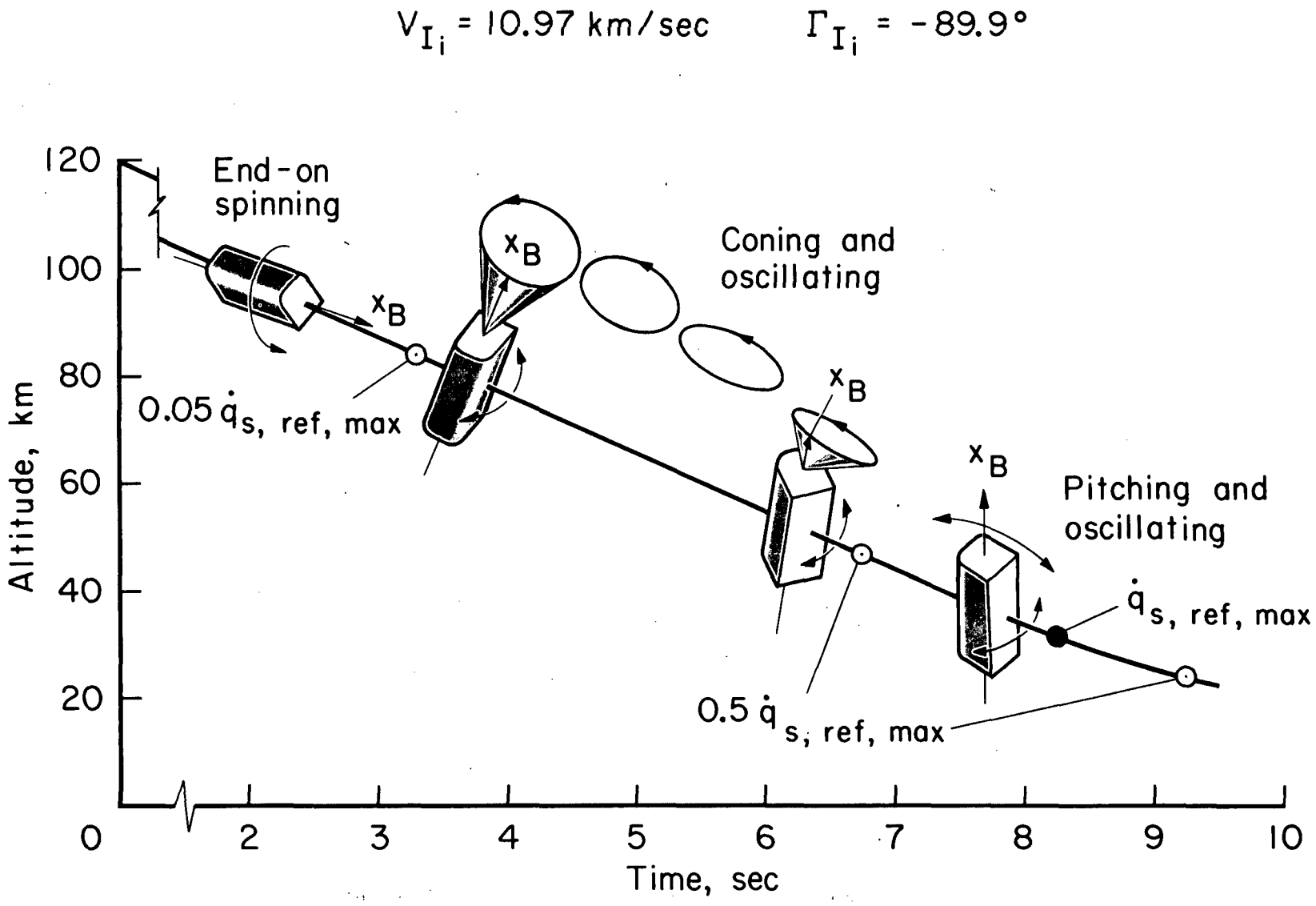

Figure 7.– Motion relative to reference heating rate during superorbital entry with Isoloaf initially spinning end-on.

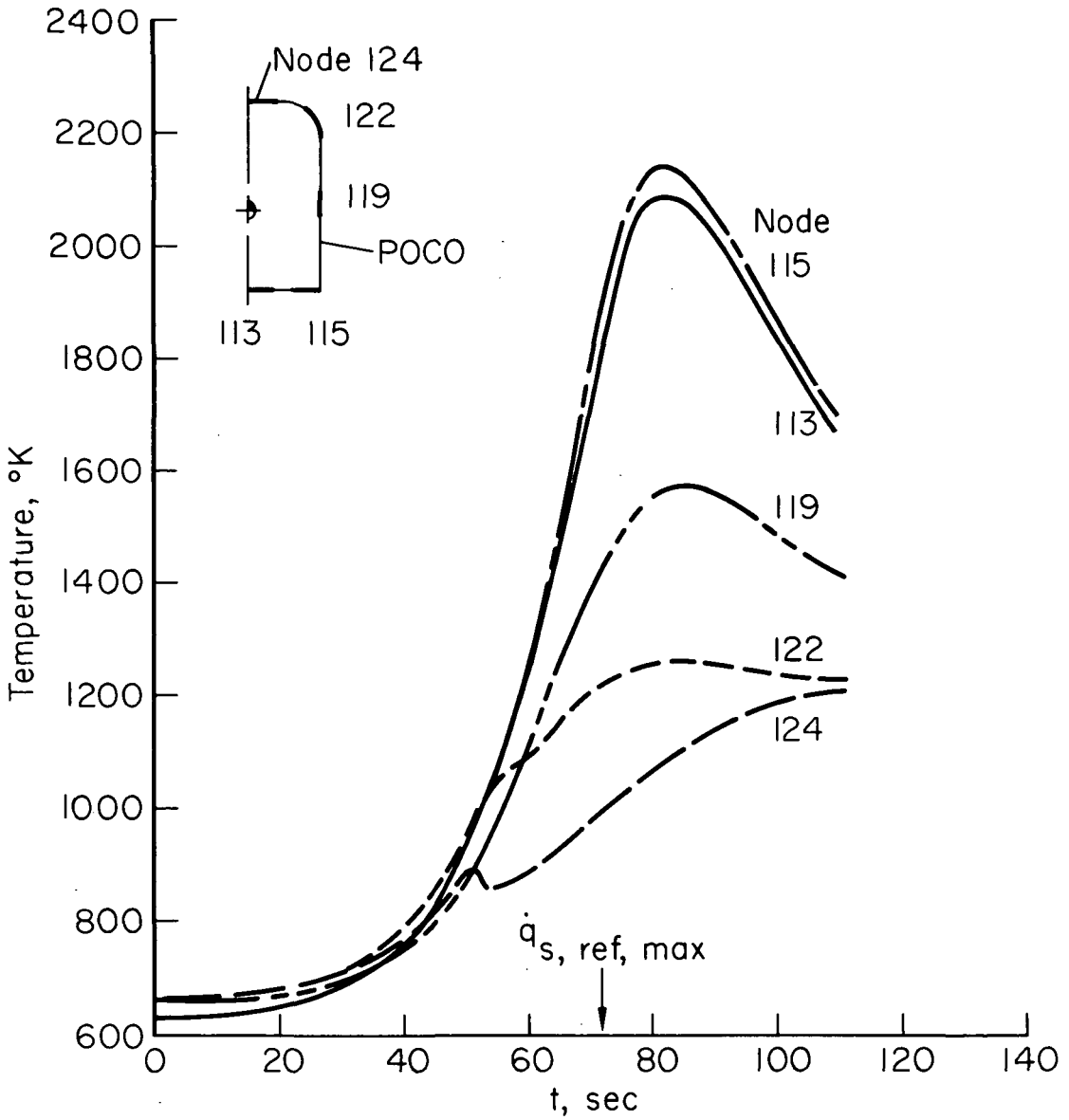

Figure 8.— Isoloaf external-surface temperature time histories during launch-abort case 1; gaps outside clad evacuated.

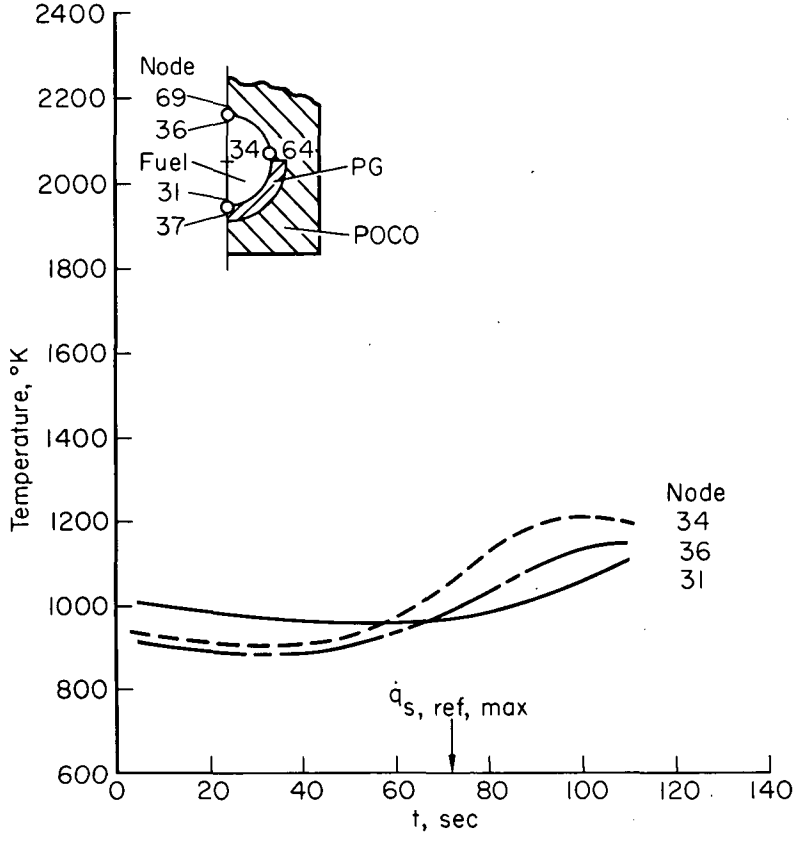

(a) Clad surface.

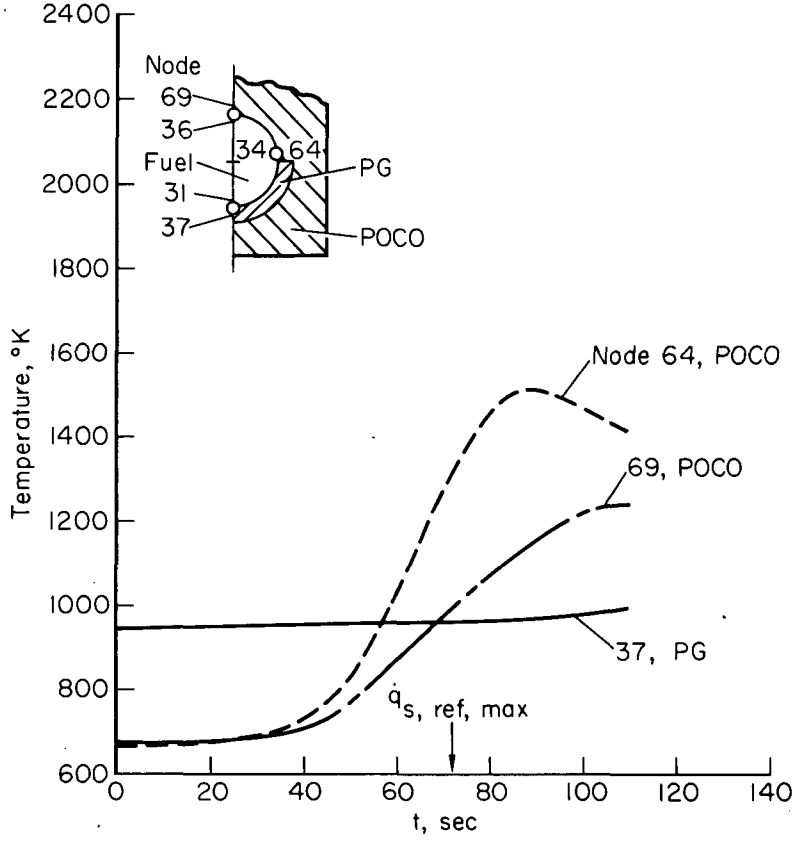

(b) Graphite surfaces.

Figure 9.– Isoloaf internal-surface temperature time histories during launch-abort case 1; gaps outside clad evacuated.

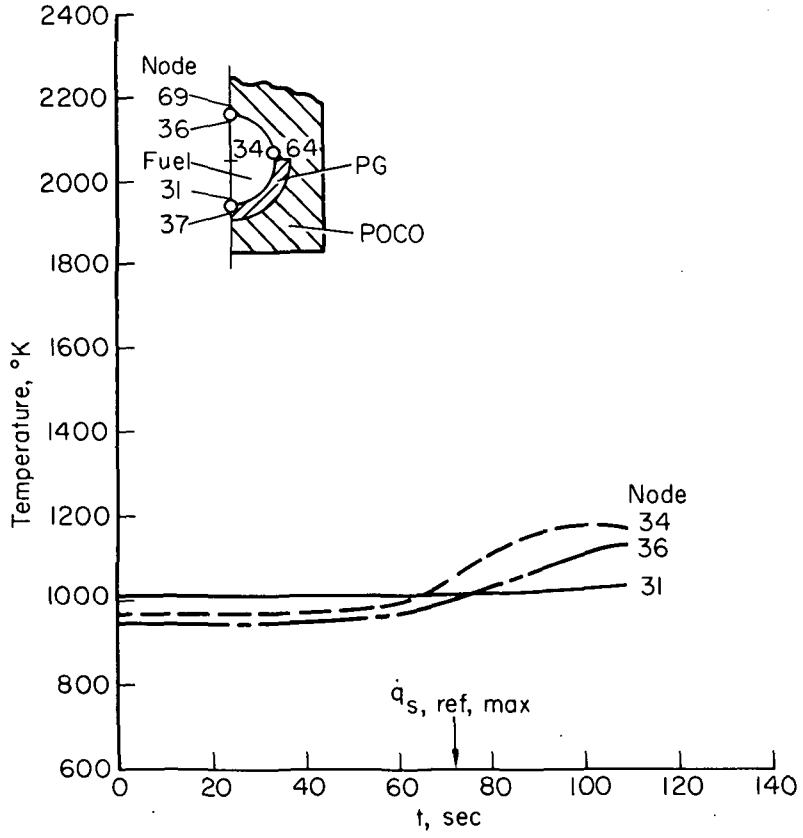

(a) Clad surface.

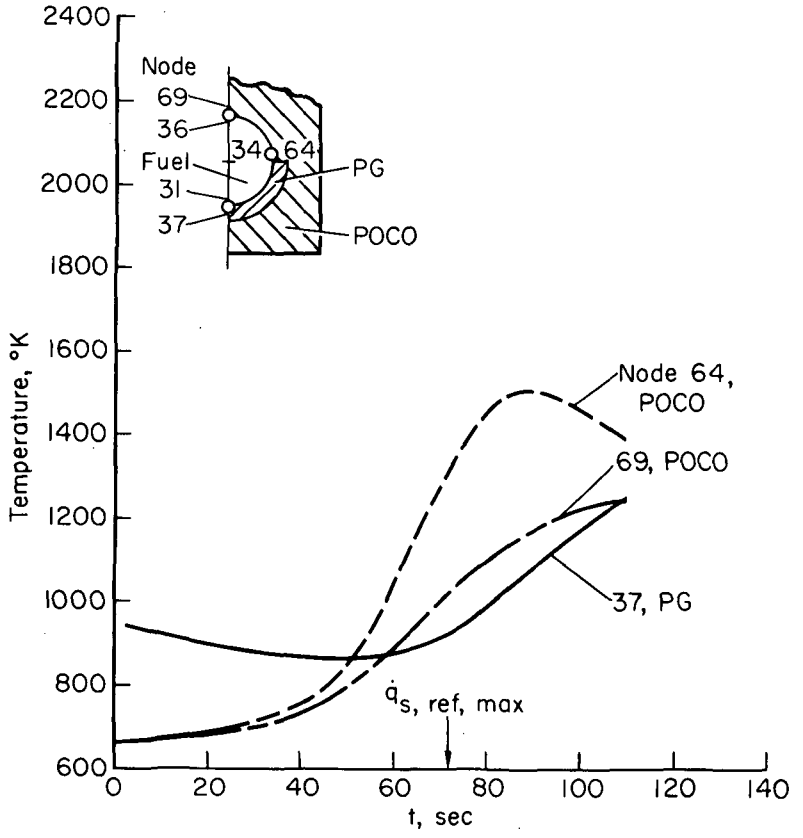

(b) Graphite surfaces.

Figure 10.– Isoloaf internal-surface temperature time histories during launch-abort case 1; gaps outside clad air filled.

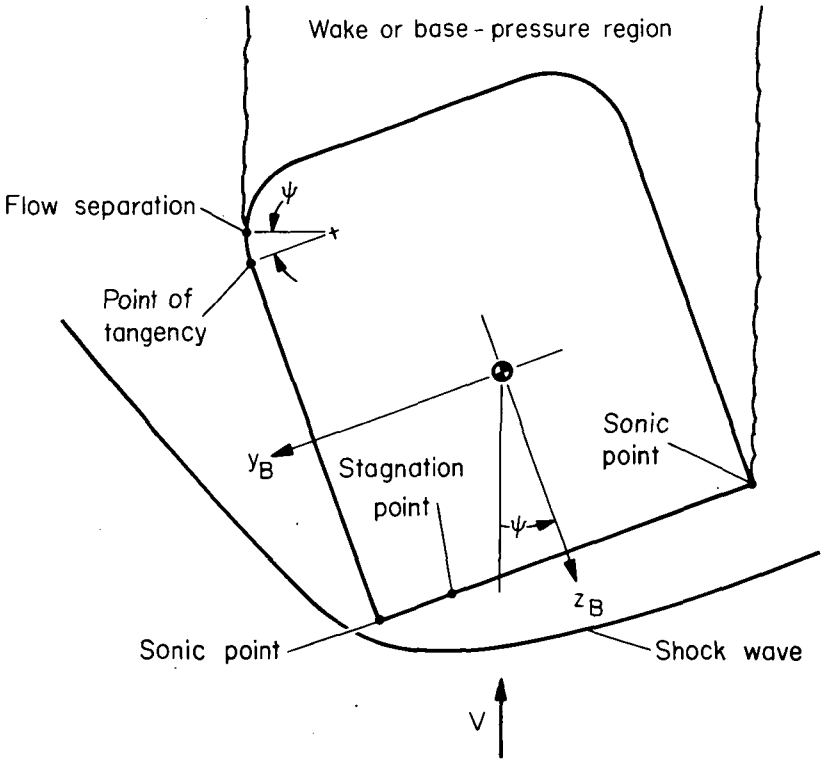

Figure 11.– Sample flow field model; $\sigma = 90°$, $\psi = 20°$.

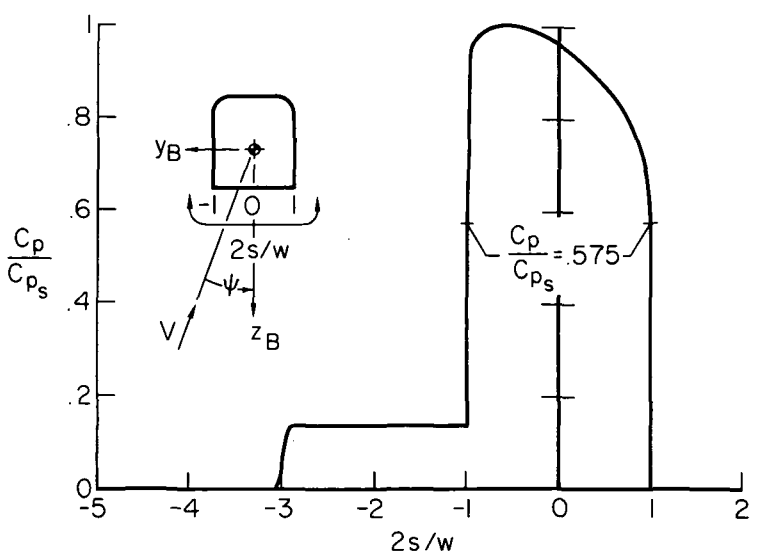

Figure 12.– Sample pressure-coefficient distribution; $\sigma = 90°$, $\psi = 20°$.

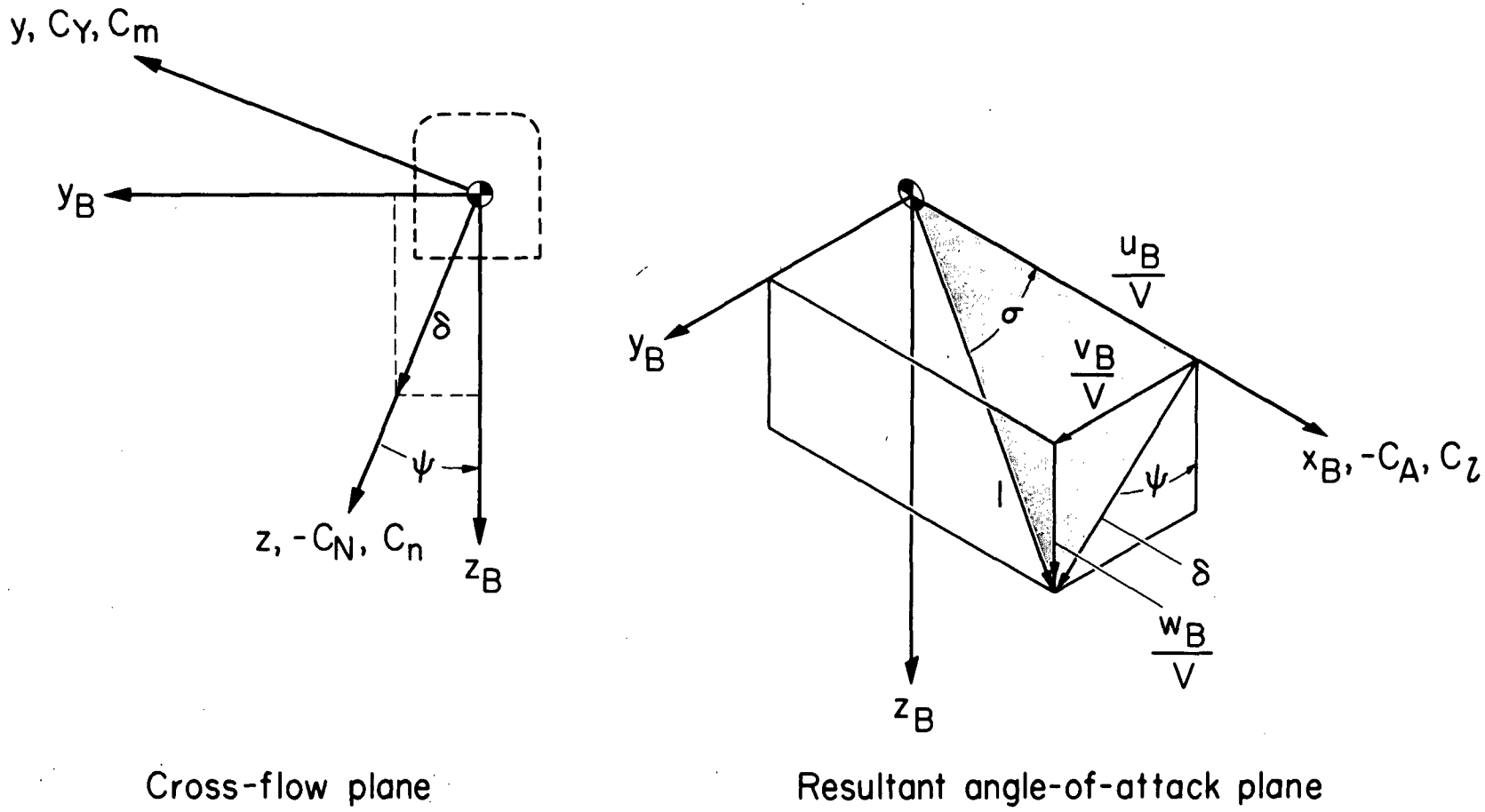

Figure 13.– Axes, angles, velocity components, and aerodynamic coefficients in the crossflow and resultant angle-of-attack planes.

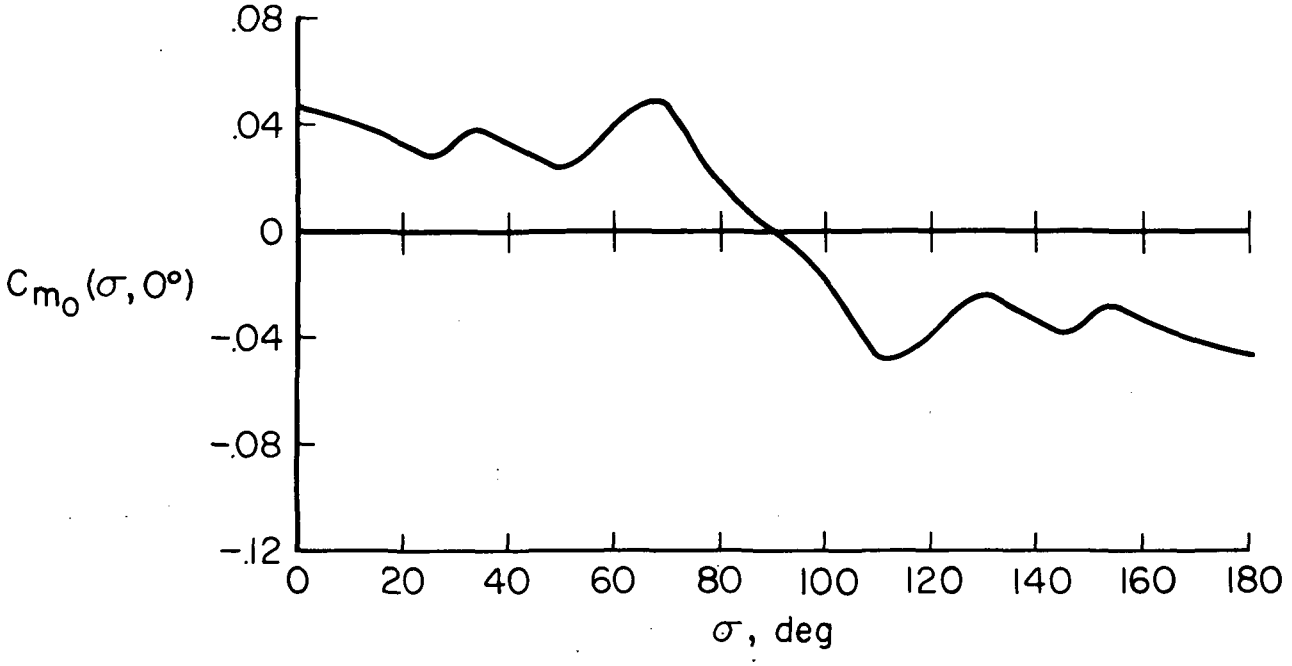

(a) Pitching-moment coefficient, $\psi = 0°$.

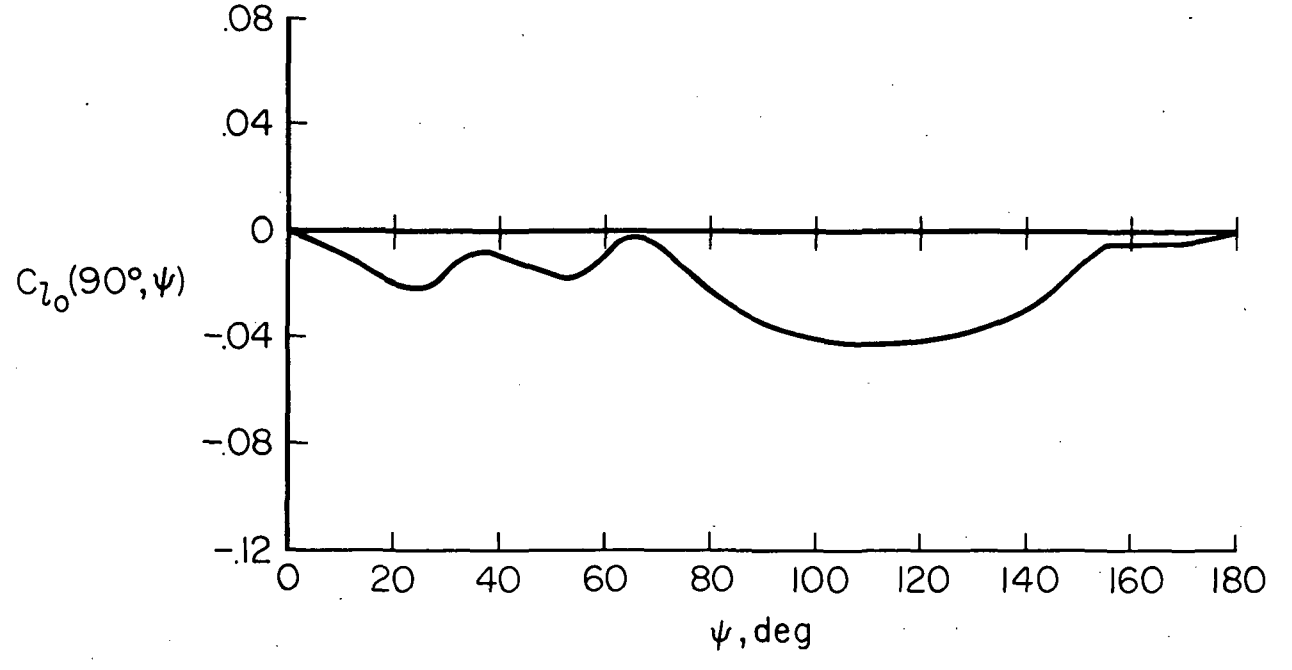

(b) Rolling-moment coefficient, $\sigma = 90°$.

Figure 14.– Static-moment coefficients for the Isoloaf due to angular displacements in the two planes of mirror symmetry.

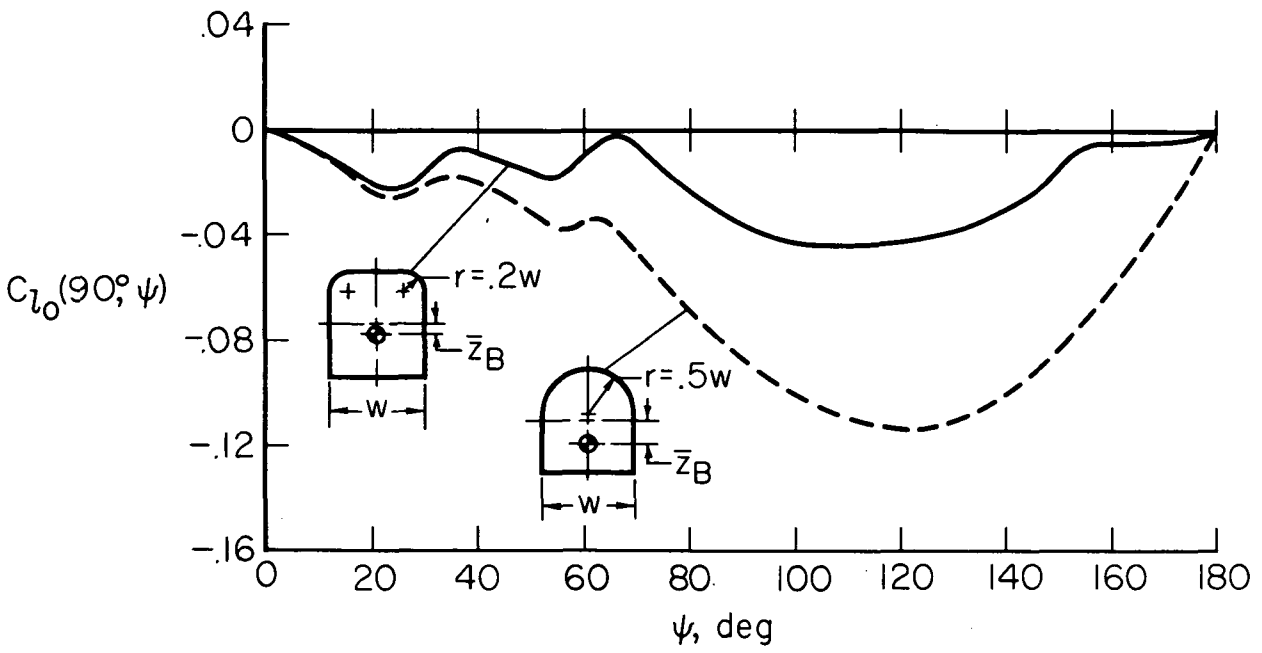

Figure 15.– Rolling-moment coefficients in the side-on attitude for two Isoloaf designs with $\bar{z}_B = 0.5r$.

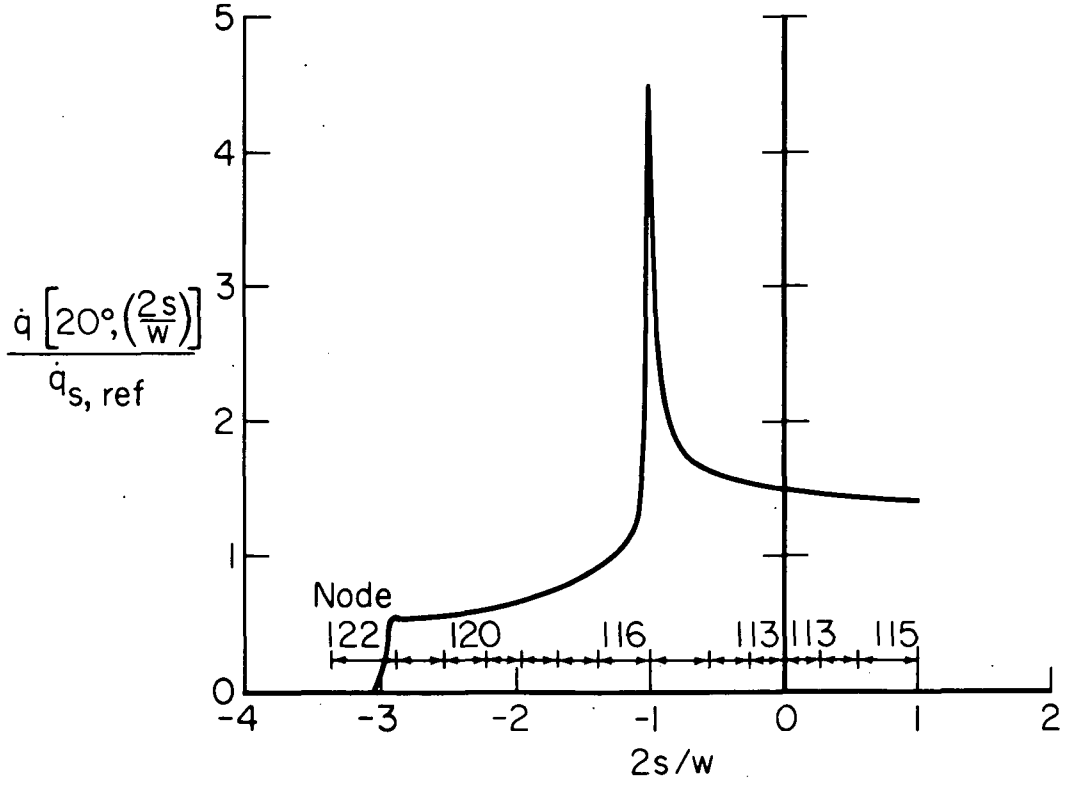

Figure 16.– Sample heating-rate distribution; $\sigma = 90°$, $\psi = 20°$.

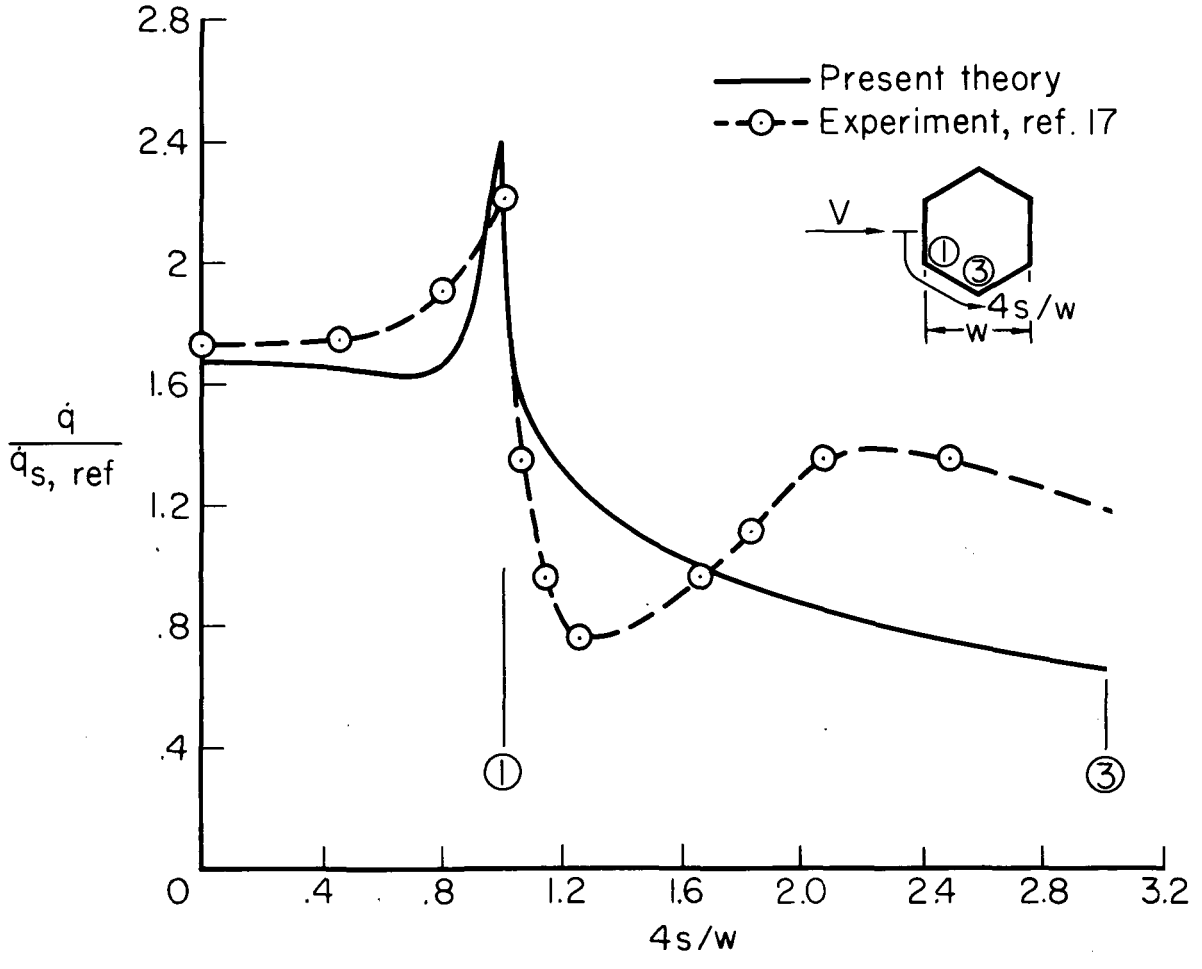

Figure 17.– Theoretical and experimental heating-rate distributions for a Pioneer-type heat-source at Mach number 6; $\sigma = 90°$, flat face forward.

NASA-Langley, 1972 — 1 A–4342

"The aeronautical and space activities of the United States shall be conducted so as to contribute . . . to the expansion of human knowledge of phenomena in the atmosphere and space. The Administration shall provide for the widest practicable and appropriate dissemination of information concerning its activities and the results thereof."

—NATIONAL AERONAUTICS AND SPACE ACT OF 1958

NASA SCIENTIFIC AND TECHNICAL PUBLICATIONS

TECHNICAL REPORTS: Scientific and technical information considered important, complete, and a lasting contribution to existing knowledge.

TECHNICAL NOTES: Information less broad in scope but nevertheless of importance as a contribution to existing knowledge.

TECHNICAL MEMORANDUMS: Information receiving limited distribution because of preliminary data, security classification, or other reasons.

CONTRACTOR REPORTS: Scientific and technical information generated under a NASA contract or grant and considered an important contribution to existing knowledge.

TECHNICAL TRANSLATIONS: Information published in a foreign language considered to merit NASA distribution in English.

SPECIAL PUBLICATIONS: Information derived from or of value to NASA activities. Publications include conference proceedings, monographs, data compilations, handbooks, sourcebooks, and special bibliographies.

TECHNOLOGY UTILIZATION PUBLICATIONS: Information on technology used by NASA that may be of particular interest in commercial and other non-aerospace applications. Publications include Tech Briefs, Technology Utilization Reports and Technology Surveys.

Details on the availability of these publications may be obtained from:

SCIENTIFIC AND TECHNICAL INFORMATION OFFICE

NATIONAL AERONAUTICS AND SPACE ADMINISTRATION

Washington, D.C. 20546